2010-08-30

Development of a Pseudo-uniform Structural Velocity Metric for Use in Active Structural Acoustic Control

Jeffery M. Fisher
Brigham Young University - Provo

BYU ScholarsArchive Citation

Fisher, Jeffery M., "Development of a Pseudo-uniform Structural Velocity Metric for Use in Active Structural Acoustic Control" (2010). *All Theses and Dissertations*. 2243.
https://scholarsarchive.byu.edu/etd/2243

Development of a Pseudo-uniform Structural Velocity Metric for use in Active Structural Acoustic Control

Jeffery M. Fisher

A thesis submitted to the faculty of
Brigham Young University
in partial fulfillment of the requirements for the degree of

Master of Science

Jonathan D. Blotter, Chair
Scott D. Sommerfeldt
Kent L. Gee

Department of Mechanical Engineering

Brigham Young University

December 2010

ABSTRACT

Development of a Pseudo-uniform Structural Velocity Metric
for use in Active Structural Acoustic Control

Jeffery M. Fisher

Department of Mechanical Engineering

Master of Science

Active control of sound and vibration fields has become an strong area of research over the past few decades. In regards to the active control of acoustic radiation from vibration fields, known as active structural acoustic control (ASAC), there have been many different methods employed to understand structural and acoustic relationships and to control vibrations to limit the acoustic radiation. With active sound field control, sensors, usually microphones, need to be dispersed in the sound field, or an array of microphones must be placed directly in the sound field which, in many cases, uses up too much space for practical applications. To remedy this, objective functions have been transferred to the structure, sensing vibrations rather than pressures. A small, integrated array of structural sensors can be placed on the structure, reducing the system's overall footprint.

Acoustic energy density has become a well established objective function, which produces a more global effect using only a local measurement. Another benefit of acoustic energy density lies in the breadth of sensor placement. While acoustic energy density has proven successful in active noise control (ANC), the quantity deals with pressures, not surface vibrations. The problem with ASAC is that an objective function with the robustness of acoustic energy density does not yet exist. This thesis focuses on a structural error sensing technique that mimics the properties of acoustic energy density control in the sound field. The presented structural quantity has been termed V_{comp}, as it is a composite of multiple terms associated with velocity. Both analytical and experimental results with the control of this quantity are given for a rectangular plate. The control of Vcomp is compared to other objective function including squared velocity, volume velocity and acoustic energy density. In the analytical cases, the benefits include: control at higher structural modes, control largely independent of sensor location, and need for only a single point measurement of squared Vcomp with a compact sensor. The control at higher frequencies can be explained by the control of multiple acoustic radiation modes. Experimental results offer some validity to the analytical benefits but alternate sensing techniques need to be investigates to more fully validate these benefits.

Keywords: ASAC, ANC, structural control, velocity control, active control of structures, Fisher

ACKNOWLEDGMENTS

First and foremost, I would like to thank all those who have contributed in any way to the completion of this thesis. I would especially like to thank my graduate committee chair, Jonathan Blotter, and members, Kent Gee and Scott Sommerfeldt. Without their continued support and excitement about this work, the obstacles encountered would have been much more difficult to overcome. Their knowledge about the subjects of this research proved invaluable as they provided useful insights into accomplishing the research presented in this thesis.

Although their help proved useful in many situations, I would like to thank my one true companion, my wife Kira, who continued supporting me when things became more difficult. Her constant confidence in me helped me push forward and overcome the obstacles and challenges which presented themselves. She spent many nights alone with our newborn baby, Luke, while I toiled away. I would lastly look heavenward as I recognize many instances in my research where moments of inspiration helped me overcome challenges along the way. Thank you all for your continued support.

TABLE OF CONTENTS

LIST OF TABLES

LIST OF FIGURES

1 INTRODUCTION

This chapter presents a brief introduction into active structural acoustic control (ASAC) to provide a context for the thesis problem statement. Goals and objectives are also presented with an outline of the remaining chapters given as well.

1.1 Active Structural Acoustic Control

Active control of sound and vibration fields has become an increasingly strong research area, with a large portion of the research focusing on different sensing techniques. In regards to the active control of sound radiation from vibrating structures, known as active structural acoustic control (ASAC), there have been many different methods employed to understand and control vibrations to limit the acoustic radiation. With the active control of sound fields, there have been large advances in the understanding of both active control mechanisms and wave interaction. In the case of ASAC, this knowledge is beginning to surface.

The theory of both ANC and ASAC relies on the superposition of waves, modal control and modal rearrangement. Propagating waves can interfere, producing an increase or decrease in sound or vibration levels. This field of research is ongoing and is gaining interest. The components of an ASAC system include, but are not limited to those shown in Figure 1-1 and explained in Table 1-1. These components form a simple hierarchy with the target structure producing the reference signal and the single sensed by the error sensor. During control, the error sensor, controller and control actuators work in a loop to minimize the error at the sensor.

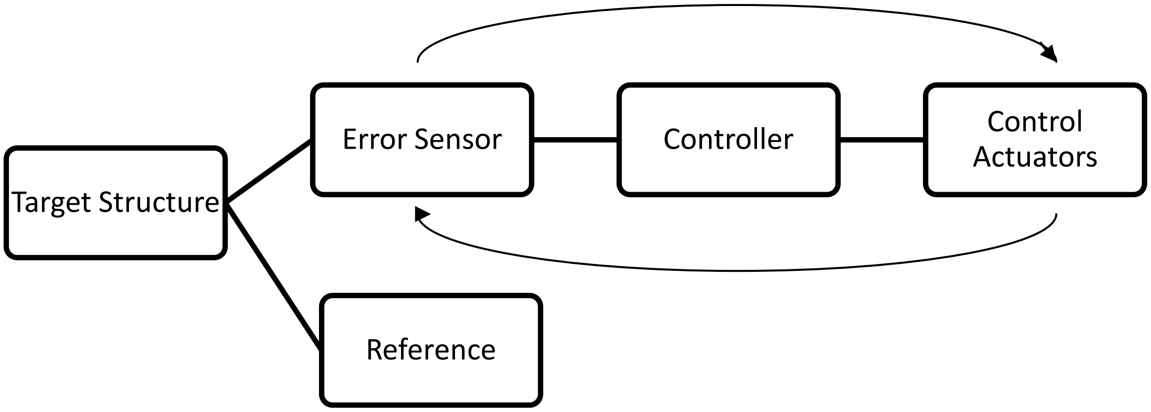

Figure 1-1: Components of an active structural acoustic control system

Table 1-1: ASAC components description

Component	Description
Target Structure	Structure from which unwanted noise radiates
Reference	Correlated with the signal to be controlled
Error sensor	Sensor which is related to the objective function, or parameter to be controlled
Controller	Software and hardware which process the reference signal and error sensor inputs and subsequently sends a control signal to the control actuators.
Control actuators	Sends out waves which cancel the signal at the error sensor

In ASAC, force actuators are applied directly to the structure to control vibration of that structure. In this lies the benefits of ASAC over traditional sound field control using a speaker arrangement: The control of sound at the source, and the system compactness. Structurally applied actuators are much less intrusive than their speaker counterparts because they can be directly applied to the structure and do not use up any space in the acoustic field, which in some cases can be very valuable such as in confined cabins. Much of the focus of ASAC is on determining the optimal objective function which will produce the best global result. Although the controller algorithms are absolutely vital to the success of the control, these algorithms have been proven in many different ANC situations. For that reason, the focus of this thesis will not be on the algorithms, but the parameter to be controlled on the target structure.

1.2 Problem Statement

ASAC is a branch of active control where, as explained previously, actuators are attached to the structure to minimize the objective function as seen by the error sensor. In both active noise control and active structural acoustic control, multiple objective functions have been used and compared by Curtis *et al.*[1] and in many instances the chosen objective function has resulted in great attenuation. As mentioned earlier, the main benefit of vibration control when compared to sound field control lies in the systems compactness. Control speakers must also be placed in the sound field, taking up valuable space in confined areas. With active sound field control, sensors, usually microphones, need to be dispersed in the sound field, or an array of microphones must be placed directly in the sound field which, in many cases, uses up too much space for practical applications. To remedy this, objective functions have been transferred to the structure, and so are related to vibrations rather than pressures. A small, integrated array of structural sensors can be placed on the structure, reducing the system's overall footprint. These structural actuators and sensors have also become less expensive, resulting in ASAC becoming a more viable and practical option when considering noise control.

The main focus in ASAC is in determining which objective function on the structure will provide the best overall global acoustic attenuation. Elliot *et al.*[2,3] investigated the effect of controlling volume velocity, but this has proven to be somewhat ineffective at higher frequencies. In addition, a large number of distributed accelerometers are required to accurately measure the volume velocity. The number of sensors required for reasonable attenuation, in many situations, is far too many for practical purposes.

While the compactness of an ASAC system is extremely beneficial, the same problems exhibited in the active control of a sound field are present in vibration control. A main issue of these systems is to determine the optimal location for both sensors and actuators. As mentioned by Sommerfeldt and Nashif[2], the optimal placement of the sensor(s) is a function of the control objective, or objective function. In the case of sound fields, the objective of controlling the acoustic energy density resolved many of the problems introduced by using the more common squared pressure approach. In dealing with ANC, a simple objective function is squared pressure at one or more microphones. While this works well in areas directly surrounding the microphone(s), other areas might see an increase in noise level. Squared pressure often does not produce the overall global effect many would like to see. Acoustic energy density has become a well established objective function, which produces a more global effect. Another benefit of acoustic energy density lies in the spatial range of the sensor placement. An easy example to illustrate this point is single point velocity control on a structure, which is analogous to pressure control in a sound field. If the sensor were placed at a node either on the structure or in the sound field, there would be practically no observability, which would result in control problems. If an energy density sensor were placed at this same location in the sound field, control would be observed because pressure is not the only quantity measured. While acoustic energy density has proven successful in ANC, the quantity deals with acoustic variables and not surface vibrations. The challenge associated with ASAC is that an objective function with the robustness of acoustic energy density does not yet exist.

1.3 Objective

The objective of this thesis is to better understand the structural acoustic coupling with the end goal of actively controlling the structural vibrations in a manner that reduces the overall acoustic radiation. The thesis objective will be accomplished in accordance with Table 1-2. An investigation into the relationships that exist between structural vibrations must first be understood and will be accomplished using known equations, as well as analytical computer modeling. Second, an investigation into structural metrics, which have a strong influence on the acoustic field, will be performed using analytical methods. Lastly, control of a structural metric and the corresponding change in the acoustic field will be preformed both analytically and experimentally.

Table 1-2: Table of objectives

Steps	Goals
Step 1	Understand relationship between the structural and acoustic fields
Step 2	Find a structural metric which, when controlled, impacts the acoustic field greatly
Step 3	Run active control both analytically and experimentally and compare results

1.4 Thesis Outline

The remainder of this thesis describes the methods used to create a structural metric, which is strongly correlated with the different modes of acoustic radiation. Chapter 2 gives an overview of ASAC and its relationship with current active noise control techniques. The next four chapters present the work completed in this thesis, including the development of a structural quantity, and analytical and experimental test cases. Chapter 3 presents the development of the new structural quantity, which is strongly correlated with the acoustic field and acoustic radiation. Chapter 4 investigates the performance of this function, in regards to acoustic radiation, when controlled structurally. Chapter 5 presents the experimental work done in regards to ASAC. Finally, Chapters presents recommendations for future work, as well as the conclusions drawn from both experimental and analytical cases.

2 BACKGROUND AND LITERATURE REVIEW

This chapter presents an in-depth look at active noise control (ANC) to build a stronger base for ASAC, as the principles are the same. Although the focus of this thesis, as explained previously, is on the objective function and not the algorithm used, it is pertinent to introduce the algorithm and give a brief description of its implementation. Common practices relating to active noise control are discussed. Additionally, previous ASAC control techniques, along with their corresponding benefits and limitations are given.

2.1 FXLMS Algorithm

The filtered-*x* least mean squares (FXLMS) algorithm has been reported in many active control systems to be the predominant algorithm[4]. This section gives a brief overview of this algorithm with a more extensive review given by Thomas[5].

In the remainder of this thesis, a feed-forward FXLMS algorithm will be used. This type of implementation relies on a reference signal, related to the unwanted noise or vibrations, being directly fed into the algorithm in order to predict the correct control signal output to control this unwanted noise. In order to visualize the process of the FXLMS feed forward implementation, a basic block diagram is given in Figure 2-1.

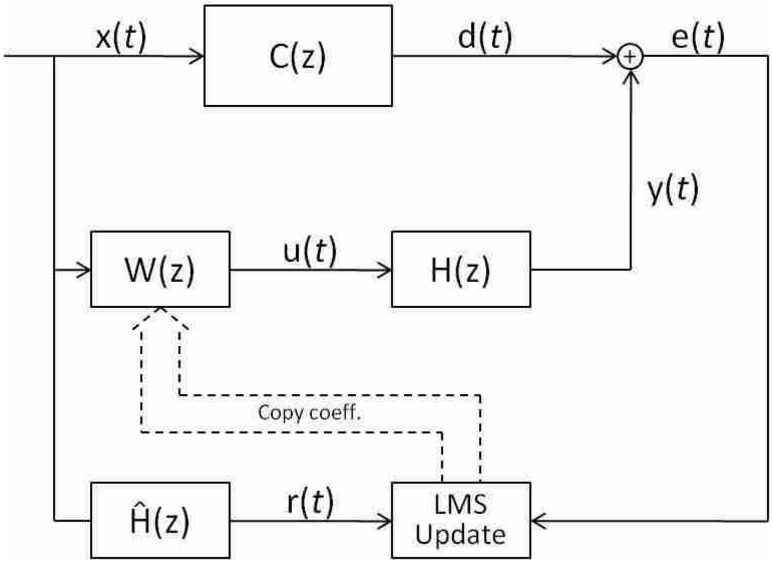

Figure 2-1: Block diagram of the FXLMS algorithm

In this diagram, *t* represents a specific discrete time index, x(t) is the reference signal, d(t) is the desired signal to be controlled, u(t) is the control signal, y(t) is the output signal, r(t) is the filtered-x signal, and e(t) is the error signal. C(z) is the frequency response of the plant, W(z) represents the adaptive filter, H(z) is the frequency response of the actual secondary path, and Ĥ(z) is the estimated secondary path.

H(z) encompasses the control actuator transfer function, the error sensor transfer function, and the propagation path between the control actuator and error sensor locations. In other words, H(z) is the physical path through which the control signal must propagate. A prediction of this physical path must be known beforehand in order to appropriately time align the control signal output. If one assumes a time-invariant linear system, W(z) and H(z) can be interchanged. This concept leads to the use of the filtered-x signal to be used to appropriately update the control filter coefficients. This in turn allows the controller to time align itself with the signal to be canceled.

In many situations, the estimate of the control path, $\hat{H}(z)$, is determined by performing aa a priori system identification (SysID). This is performed by sending a known signal from the controller and taking the cross-correlation between the signal being sent from the controller and the signal received from the error sensor measurement. This will account for the time it takes the signal to go through any electronics to get to the control actuator, and then propagate to the error signal, and finally any processing required for the signal to reach the algorithm. The performance of the algorithm, with its intended use, relies on the error as seen by the algorithm after all processing has taken place. The convergence of this gradient-based algorithm is based on the filter coefficients, which are in turn updated by the error signal, e(t), as given by Eqs. 2.1 and 2.2.

$$W(t+1) = W(t) + \mu e(t)R(t) \tag{2.1}$$

where

$$R(t) = W(t)X(t) \tag{2.2}$$

The error, as seen by the controller, is directly related to the objective to be controlled at a particular location. In this case W, R, and X are vectors with W being a vector of coefficients, R is a vector of data and X is also a vector of data.

2.2 Objective Functions

When the control signal reaches the original disturbance, or primary signal, the measured signal is the error signal and is measured according to the objective function desired. ANC has evolved over the years in its use of the objective function. Squared pressure has proven to be an acceptable objective function and very easy to implement, but it does have some drawbacks. For example, if a pressure sensor were placed at a pressure node versus an anit-node, considerable problems in the observability of the error sensor and convergence of the algorithm would occur. Later work done by Sommerfeldt and Nashif[6] has shown that minimizing acoustic energy density tends to give more global control of the sound field. Because energy density relies on both pressure and particle velocity, it is much less dependent on sensor location. The more robust the objective function, in terms of sensitivity to sensor placement, the better the performance will tend to be.

One very desirable property of an objective function is that it be quadratic in nature. With a quadratic objective function, a single global minimum will exist. This allows gradient based algorithms to converge easily and not be hindered by local minima. For this reason, squared pressure was typically chosen as an objective function and is also why minimizing energy density works well. Both objective functions are quadratic in nature.

2.3 Literature Review

Many different control schemes have been attempted using control actuators mounted directly to the structure. There are two main methods of ASAC, as explained by Snyder and Hansen[7]. One way is to increase the impedance of the structural modes thus, decreasing their amplitude. This technique is known as modal control. The second method is to alter the amplitudes and phases of the same structural modes. This is known as modal rearrangement. The purpose of modal rearrangement is either to reduce the overall vibration level of the structure or to create vibration patterns which radiate less efficiently. Portions of both modal control and modal rearrangement can be seen in different control situations. Neither one has to be the only method of control. To create a situation in which one or both of the methods of control is used, a performance function or objective function must be controlled.

However, a relationship must exist between the objective function and the radiation of the structure, otherwise, no control will be observed. The objective functions mentioned above all deal with the acoustic properties of the radiating structure or noise source. Although these objective functions deal with the acoustic properties, the control actuators have been implemented on the structure so as to control the structural vibrations, which will then reduce the acoustic objective function. This has proven effective in many situations which include controlling pressure[8,9,10]. However, the current interest has been on determining structural objective functions that will perform similarly to the acoustic objective functions. This will allow the control system to be integrated into the structure, leaving a significantly smaller footprint than traditional ANC systems.

Certain energy-based structural metrics and their influence on acoustic radiation have been investigated. A well-known quantity which has been investigated is structural intensity, or structural power flow. However, it has been shown that structural power flow has little effect on acoustic intensity[11] and thus shows little promise as a control metric. Elliot *et al.*[2,3] investigated the effect of controlling volume velocity, but this has proven somewhat ineffective at higher frequencies and has been shown to require a large number of transducers in order to accurately measure the volume velocity. The number of sensors required to estimate the volume velocity in many situations is far too many for practical purposes. The control of acoustic radiation modes using structural sensors has shown promise, but requires the use of multiple sensors and knowledge of the radiation modes that contribute significantly to the overall radiation.[12,13,14]

3 DEVELOPMENT OF COMPOSITE VELOCITY

The purpose of this chapter is to explain the basis behind a new structural quantity, V_{comp}, developed specifically for use in ASAC situations.

3.1 Volume Velocity

Focusing on the relationship between structural vibrations and acoustic radiation brings out two relatively well known concepts. The first of these is the concept of volume velocity. Research has suggested that most of the acoustic radiation from a structure is attributed to the more global quantity of volume velocity[2,3,13,15]. This can be viewed from Rayleigh's integral given as

$$p(\boldsymbol{r},t) = \frac{j\omega\rho}{2\pi} e^{j\omega t} \int_S \frac{\tilde{v}_n(\boldsymbol{r}_s) e^{-jkR}}{R} dS \tag{3.1}$$

where p is the pressure, ω is the angular frequency in radians per second and ρ is the density of the medium through which the sound is propagating. Also, $\mathbf{r}$ is the position vector of the observation point, $\mathbf{r}_s$ is the position on the surface, having a velocity amplitude $\tilde{v}_n$ and R is the magnitude of $\mathbf{r}$-$\mathbf{r}_s$. As can be seen, a reduction in the overall level of $\tilde{v}_n$ on the structure will tend to decrease the pressure at all points in the field. Volume velocity in its most basic sense refers to the net velocity of the vibrating structure. Thus, although in some instances the amplitude of the vibration response may be greater, the volume velocity can be close to zero.

Even modes will display this property while odd modes will not. As research has shown, odd modes radiate more efficiently than even modes because they have non-zero volume velocity. This is one of the reasons that volume velocity has been strongly associated with acoustic radiation.

3.2 Acoustic Radiation Modes

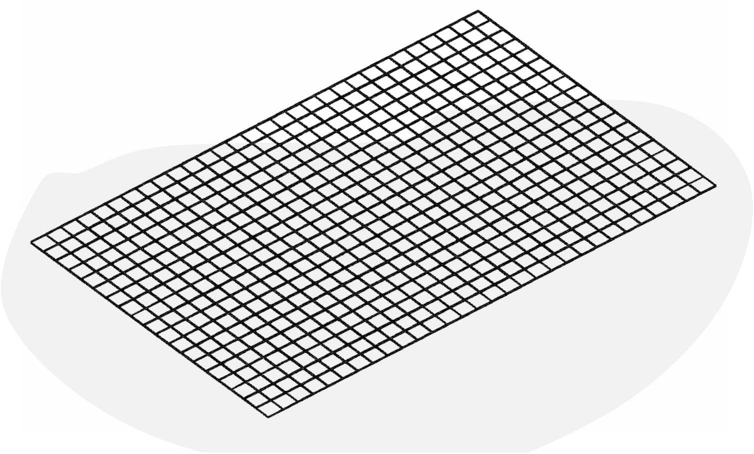

Figure 3-1: A panel divided into 19x30 piston elements.

A second relationship between structural vibrations and acoustic radiation deals with acoustic radiation modes. As explained by Fahy and Gardonio[16], these are modes which radiate independently of the structural vibrations and give deeper insight into sound radiation. The derivation given in this thesis will be derived by the elementary radiator formulation, as developed by Elliot and Johnson.[13] As shown in Figure 3-1, the panel is divided into a grid of N elements whose transverse velocities are given by $\tilde{v}_{er}$. The complete vibration of the panel can be represented by the vector in Eq. 3.2.

$$\{\tilde{v}_e\} = [\tilde{v}_{e1}\ \tilde{v}_{e2}\ \dots\ \tilde{v}_{eN}]^T \tag{3.2}$$

Using this, the total radiated sound power is given by

$$\overline{P}(\omega) = \{\tilde{v}_e\}^T[R_R]\{\tilde{v}_e\} \tag{3.3}$$

The matrix $[R_R]$ is defined as the 'radiation resistance matrix' and is given by

$$[R_R] = \frac{\omega^2\rho_0 A_e^2}{4\pi c}\begin{bmatrix} 1 & \frac{\sin(kD_{12})}{kD_{12}} & \dots & \frac{\sin(kD_{1N})}{kD_{1N}} \\ \frac{\sin(kD_{21})}{kD_{21}} & 1 & \dots & \vdots \\ \dots & \dots & \ddots & \vdots \\ \frac{\sin(kD_{N1})}{kD_{N1}} & \dots & \dots & 1 \end{bmatrix} \tag{3.4}$$

where A_e is the cross-sectional area of each individual element, D_{ij} is the distance between the i-th and j-th elements, ρ_0 is the density of air, *c* is the speed of sound in air and *k* is the wavenumber. It should be noted that the matrix $[R_R]$ is a positive definite matrix. Given the $[R_R]$ matrix in equation 3.4, the acoustic radiation modes are obtained from:

$$[R_R] = [Q]^T[\Lambda][Q] \tag{3.5}$$

where [Q] is a matrix of orthogonal eigenvectors and [Λ] is a diagonal matrix of eigenvalues. The relative efficiencies of the radiation modes are given by the elements of [Λ], and the shape of each mode is given by the corresponding row of [Q], or the eigenvectors. The shapes of the first six acoustic radiation modes for a rectangular plate are shown in Figure 3-2.

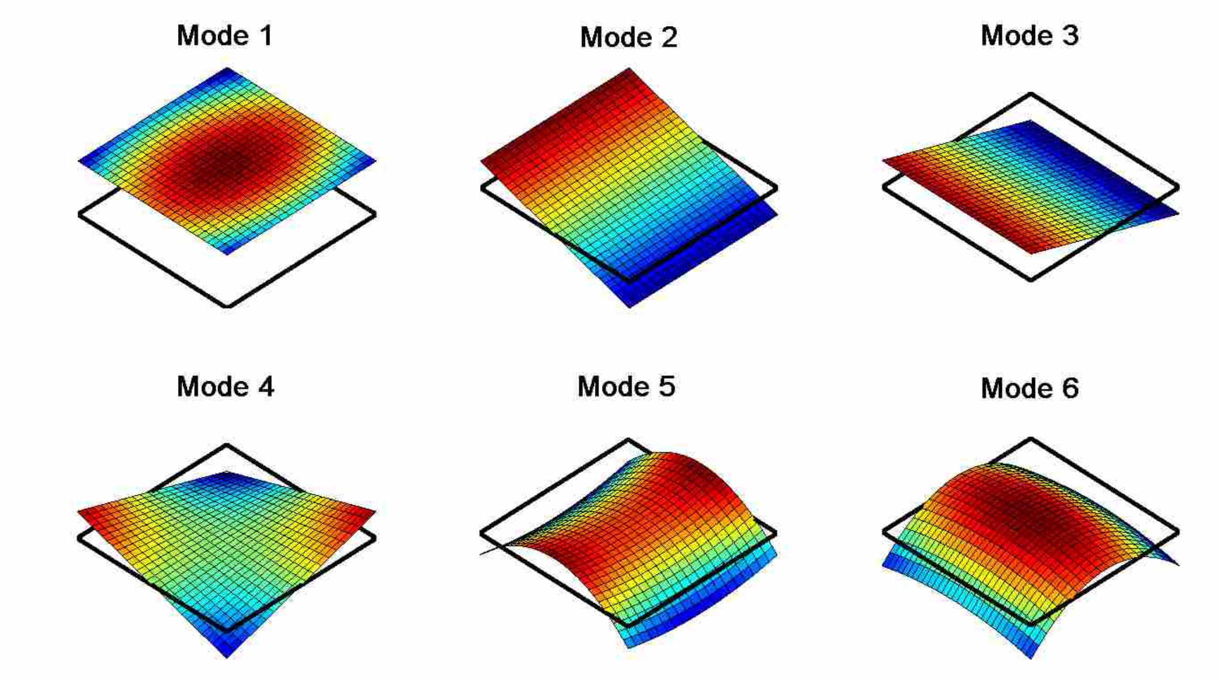

Figure 3-2: Acoustic radiation mode shapes

Using radiation modes, the overall power radiated is given by

$$\overline{P}(\omega) = \{\tilde{y}\}^H[\Lambda]\{\tilde{y}\} = \sum_{r=1}^{N} \lambda_r|\tilde{y}_r|^2 \tag{3.6}$$

$$\{\tilde{y}\} = \ [Q]\{\tilde{v}_e\} \tag{3.7}$$

Here, N is the total number of elements and λ_r and $\tilde{y}_r$ are the components corresponding to the element of interest. The shape of each radiation mode is mildly dependent on frequency. The higher the frequency, the more curvature appears in the individual radiation modes. In order to compare the relative importance of the individual radiation modes, the power radiated by the individual acoustic radiation modes is given by Eq. 3.8.

$$\overline{P}_m(\omega) = \lambda_m|\tilde{y}_m|^2 \tag{3.8}$$

with m being the index of the individual mode.

Controlling radiation modes has been an effective way to control the power radiated from a panel. However, the structural geometry associated with the vibrations must be known a priori to calculate the radiation modes and determine sensor locations that are conducive to sensing all significant radiation modes present. In most cases, structural vibrations cannot be fully mapped without equipment such as multiple accelerometer arrays or a scanning laser Doppler vibrometer, and the radiation modes cannot be obtained without some numerical analysis of the structure. Furthermore, depending on how many acoustic radiation modes are significant, these techniques can require the use of a large number of sensors which would be required to estimate the amplitudes of the significant radiation modes.

3.3 Composite Velocity Derivation

The analysis of both volume velocity and acoustic radiation modes reveals the idea that a quantity which gives a vibration field related to volume velocity as well as mimics the acoustic radiation modes should be a desirable objective function to minimize. If this effect could be created using a point sensor measurement rather than a distributed array of sensors, a global result could be achieved using a simpler sensor configuration than for the other objective functions which, as previously mentioned, can require a large distributed array of sensors to estimate their respective quantities. A quantity that represents the volume velocity as well as mimics acoustic radiation modes has been developed. This quantity takes multiple velocity states and combines them and so has been termed V_{comp} for composite velocity. The derivation and use of this term will be discussed.

After the derivation is discussed, squared V_{comp} is then used as the minimization quantity in an active control system. For the derivation of squared V_{comp}, an analytical model of a simply supported, damped, plate with multiple point force locations will be used. The displacement of the plate is given by Eqs. 3.9-3.12.

$$w(x,y) = \sum_{q=1}^{F} \frac{f_q}{\rho_s h} \sum_{m}^{\infty} \sum_{n}^{\infty} \frac{W_{mn}(x,y) W_{mn}(x_q, y_q)[\omega_{mn}^2 - \omega^2 - i\eta\omega_{mn}^2]}{[\omega_{mn}^2 - \omega^2]^2 + \eta^2 \omega_{mn}^4} \tag{3.9}$$

$$W_{mn}(x,y) = \frac{2}{\sqrt{L_x L_y}} sin\left(\frac{m\pi x}{L_x}\right) sin\left(\frac{n\pi y}{L_y}\right) \tag{3.10}$$

$$\omega_{mn} = \sqrt{\frac{D}{\rho_s h}} \left(\frac{m^2\pi^2}{L_x^2} + \frac{n^2\pi^2}{L_y^2}\right) \tag{3.11}$$

$$D = \frac{Eh^3}{12(1-\nu^2)} \tag{3.12}$$

where f_q is the amplitude of the qth driving force, $\rho_s$is the density of the plate material, E is Young's modulus, ν is Poisson's ratio, h is the plate thickness, and L_x and L_y are the plate dimensions. The structural damping ratio is given by η, ω is the driving frequency in radians, and m and n are structural mode shape numbers. The plate properties are given in Table 3-1 and the first fifteen structural modes of the plate, as computed by Eq. 3.11, are given in Table 3-2.

Table 3-1: Material properties of plate

Property	Value
Length (*x* direction) (L_x)	0.438 m
Length (*y* direction) (L_y)	0.762 m
Thickness (h)	0.001 m
Young's Modulus (E)	207 X 10^9 Pa
Poisson's Ratio (ν)	0.29
Density (ρ)	7800 kg/m^3
Damping ratio (η)	0.1%

Table 3-2: Resonant frequencies of a simply supported plate

Mode	*Modal frequency Hz*
(1,1)	13.390
(2,1)	24.889
(1,2)	42.059
(3,1)	44.055
(2,2)	53.559
(4,1)	70.888
(3,2)	72.725
(1,3)	89.841
(4,2)	99.557
(2,3)	101.341
(5,1)	105.386
(3,3)	120.507
(5,2)	134.056
(4,3)	147.339
(6,1)	147.552

For the (1,1) mode of the plate, excited by a single point force at an anti-node, four velocity terms were computed. These correspond to the squared transverse, rocking and twisting velocities, given by

$$\left(\frac{dw}{dt}\right)^2,\left(\frac{d^2w}{dxdt}\right)^2,\left(\frac{d^2w}{dydt}\right)^2,\left(\frac{d^3w}{dxdydt}\right)^2 \tag{3.13}$$

and normalized plots of these quantities are given in Figure 3-3. Values for each of these terms will be discussed later and are not given in the above figure. Equations for these four terms are given in Eqs. 3.14-3.17.

$$\frac{dw}{dt}(x,y)=\sum_{q=1}^{F}\frac{f_q}{\rho_s h}\sum_{m}^{\infty}\sum_{n}^{\infty}\frac{W_{mn}(x,y)W_{mn}(x_q,y_q)[\omega_{mn}^2-\omega^2-i\eta\omega_{mn}^2]}{[\omega_{mn}^2-\omega^2]^2+\eta^2\omega_{mn}^4}i\omega \tag{3.14}$$

$$\begin{aligned}&\frac{d^2w}{dxdt}(x,y)\\&=\sum_{q=1}^{F}\frac{f_q}{\rho_s h}\sum_{m}^{\infty}\sum_{n}^{\infty}\frac{\frac{2}{\sqrt{L_xL_y}}cos\left(\frac{m\pi x}{L_x}\right)sin\left(\frac{n\pi y}{L_y}\right)W_{mn}(x_q,y_q)[\omega_{mn}^2-\omega^2-i\eta\omega_{mn}^2]}{[\omega_{mn}^2-\omega^2]^2+\eta^2\omega_{mn}^4}\left(\frac{m\pi}{L_x}\right)i\omega\end{aligned} \tag{3.15}$$

$$\frac{d^2w}{dydt}(x,y) = \sum_{q=1}^{F}\frac{f_q}{\rho_s h}\sum_{m}^{\infty}\sum_{n}^{\infty}\frac{\frac{2}{\sqrt{L_xL_y}}\, sin\left(\frac{m\pi x}{L_x}\right) cos\left(\frac{n\pi y}{L_y}\right) W_{mn}(x_q,y_q)[\omega_{mn}^2-\omega^2-i\eta\omega_{mn}^2]}{[\omega_{mn}^2-\omega^2]^2+\eta^2\omega_{mn}^4}\left(\frac{n\pi}{L_y}\right)i\omega \tag{3.16}$$

$$\frac{d^3w}{dxdydt}(x,y) = \sum_{q=1}^{F}\frac{f_q}{\rho_s h}\sum_{m}^{\infty}\sum_{n}^{\infty}\frac{\frac{2}{\sqrt{L_xL_y}}\, cos\left(\frac{m\pi x}{L_x}\right) cos\left(\frac{n\pi y}{L_y}\right) W_{mn}(x_q,y_q)[\omega_{mn}^2-\omega^2-i\eta\omega_{mn}^2]}{[\omega_{mn}^2-\omega^2]^2+\eta^2\omega_{mn}^4}\left(\frac{m\pi}{L_x}\frac{n\pi}{L_y}\right)i\omega \tag{3.17}$$

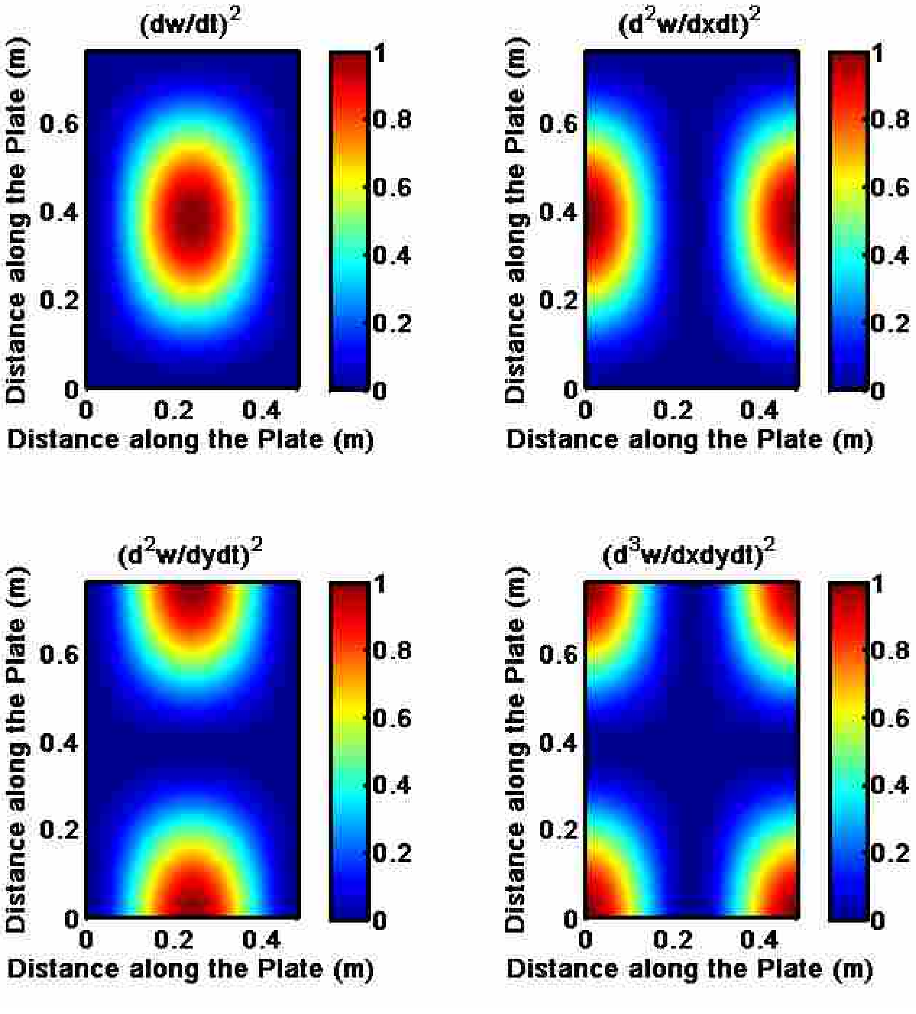

Figure 3-3: Velocity terms visualization for the (1,1) mode

Considering these four velocity terms and referring to Figure 3-3, each of the four terms given is dominant in a different spatial portion of the plate, and with a combination of these terms, a fairly uniform velocity field can be developed. Also, referring to these four quantities and the first four acoustic radiation modes given in Figure 2, a commonality exists between the two. The first radiation mode can be viewed as a transverse velocity, the second a rocking velocity in x, the third a rocking velocity in y, and the fourth, a twisting velocity. Squared V_{comp} was derived using a combination of these four terms, which provides the most uniform field over the entire plate. In order to combine these four terms, a simple linear combination was performed as given by

$$\left(V_{comp}\right)^2 = \alpha\left(\frac{dw}{dt}\right)^2 + \beta\left(\frac{d^2w}{dxdt}\right)^2 + \gamma\left(\frac{d^2w}{dydt}\right)^2 + \delta\left(\frac{d^3w}{dxdydt}\right)^2 \tag{3.18}$$

As can be seen by Eqs. 3.14-3.17, the maximum values of each term will vary with a standard scaling value based on the size of the plate as well as the structural mode at which the plate is vibrating. Table 3-3 gives the standard scaling values for each of the terms, which when multiplied by the given quantity, will create a maximum value equal to that of the transverse velocity.

Table 3-3: Structural quantity scaling factors

Quantity	$\boldsymbol{\frac{dw}{dt}}$	$\boldsymbol{\frac{d^2w}{dxdt}}$	$\boldsymbol{\frac{d^2w}{dxdt}}$	$\boldsymbol{\frac{d^2w}{dxdt}}$
Factor	1	$\left(\boldsymbol{\frac{L_x}{m\pi}}\right)^2$	$\left(\boldsymbol{\frac{L_y}{n\pi}}\right)^2$	$\left(\boldsymbol{\frac{L_xL_y}{mn\pi^2}}\right)^2$

To determine the optimal values for α, β, γ and δ, these scaling factors can be used by treating α as a known value and then scaling the other factors accordingly. Values for α, β, γ,and δ, with an arbitrary α value, are given for any structural mode *(m,n)* and plate dimensions in

Table 3-4. Also given in Table 3-4 in brackets are the units associated with each scaling factor as the overall units of squared V_{comp} will be velocity squared and in this case will be $(m/s)^2$.

Table 3-4: α,β,γ, and δ Scaling factors

α	β $[m^2]$	γ $[m^2]$	δ $[m^4]$
α	$\alpha\left(\frac{L_x}{m\pi}\right)^2$	$\alpha\left(\frac{L_y}{n\pi}\right)^2$	$\alpha\left(\frac{L_x L_y}{mn\pi^2}\right)^2$

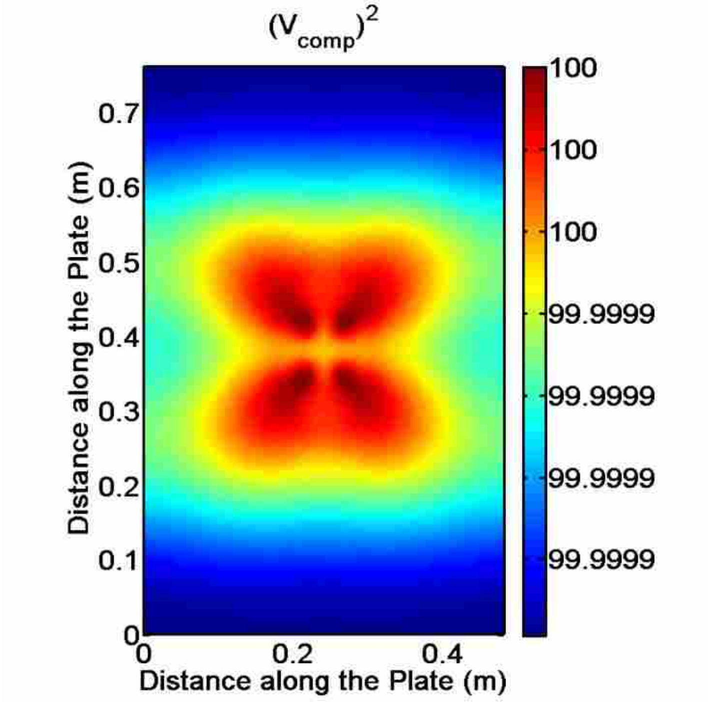

Figure 3-4: Squared V_{comp} using scaled velocity terms

Using these scaling values, the analytically computed squared V_{comp} for the (1,1) structural mode is shown in Figure 3-4 and it should be noted that the quantity was multiplied by one hundred to show the difference in the color scale. Squared V_{comp} was normalized by its maximum value to show a somewhat general case. The scale verifies that the squared V_{comp} computation for this mode, using the relative coefficients, gives a uniform value over the entire plate. A simpler way to look at the scaling values is if the terms were to be normalized by their own maximum value or normalized so their maximum values were equal. Then, all of the scaling factors would be equal values. The values for the scaling factors used in the following analytical calculations are given in Table 3-5.

Table 3-5: Average α,β,γ, and δ values for the first fifteen structural modes

α	β	γ	δ
1.0	0.01211	.01717	1.8654e-4

4 ANALYTICAL COMPARISON

This chapter presents analytical results based on using squared V_{comp} as an objective function. A comparison to other objective functions is also presented.

4.1 Radiated Power

In order to compare levels of acoustic radiation, the value of radiated power was chosen as the benchmark and was calculated using the elementary radiator method given by Johnson and Elliot[13]. This method involves breaking the structure into a spatial grid of small acoustic radiators as shown in Figure 3-1. This particular method was selected because of the ease of calculating the acoustic radiation modes as well. The power radiated from a plate using elementary radiators is given by Eq. 4.1.

$$\overline{\mathrm{P}}(\omega) = \{\tilde{\mathrm{v}}_{\mathrm{e}}\}^{\mathrm{H}}[\mathrm{R}]\{\tilde{\mathrm{v}}_{\mathrm{e}}\} \tag{4.1}$$

where $\{\tilde{\mathrm{v}}_{\mathrm{e}}\}$ is a velocity vector containing the velocities of the individual elements and [R] is the 'radiation resistance matrix' shown in Eq. 3.4.

Using the analytical model previously mentioned, a primary force location, a control force location, and a sensor location were chosen. The locations of the actuators are given in Table 4-1, with the sensor location to be given later.

Table 4-1: Force actuator locations

Actuator	Location
Primary disturbance force	(0.083,0.629)
Control force	(0.083,0.127)

With the objective function being squared V_{comp}, the optimal magnitude and phase of the control force was determined by using a simple gradient based algorithm, which minimized the objective function at the error sensor location. Once the controlled velocity field was established, the radiated powers from both the controlled and uncontrolled cases were compared.

In order to provide a separate control benchmark, squared velocity, volume velocity estimate, and acoustic energy density were also used as objective functions. Squared velocity was chosen because of its ease of implementation in experimental cases as well as its ability to give useful insights into structural and acoustic relationships. Both volume velocity and acoustic energy density were chosen based on their highly referenced use in the literature as well as to provide one of the better control objectives in ANC, acoustic energy density, which is currently used in practical applications[17]. An approximation was used for the volume velocity where the number of points used to acquire a good estimate of the volume velocity was based on work by Sors and Elliott[7] and is given by

$$N = \frac{5}{3\pi} c_o l \sqrt{\frac{m}{D}} \tag{4.2}$$

where c_o is the speed of sound, m is the mass per unit area, D is the bending stiffness, and l is the smallest plate dimension. For this specific case, the approximate number of sensors is 62. This number is not practical for experimental purposes. However, 60 points were used in the analytical case with ten equally distributed sensors in the y-direction and six in the x-direction.

In the case of acoustic energy density control, the plate was placed on the wall of a room with dimensions 5.70m X 2.50m X 4.30m. The plate was placed towards the center of the wall with dimensions 5.70m X 2.50m, with the offset from the corner of the room to the lower left corner of the plate being 2.59m X 0.89m. The equation for acoustic energy density is given by

$$w = \frac{p^2}{2\rho c^2} + \frac{1}{2}\rho u_x^2 + \frac{1}{2}\rho u_y^2 + \frac{1}{2}\rho u_z^2 \tag{4.3}$$

where p is the pressure at the measurement point, ρ is the density of air, c is the speed of sound in air and u_x, u_x and u_x are the velocities in their respective directions. The velocities in the orthogonal directions can be obtained using Euler's equation, given in Eq. 4.4, when pressures on both sides of the measurement point are known.

$$\rho \frac{du}{dt} = -\nabla p \tag{4.4}$$

This approach was taken in determining the energy density at a point. The pressure at any point in the room is given by Eqs. 4.5-4.8.

$$p(x,y,z,\omega) = j\frac{k\rho c}{V} Q(\omega) \sum_{N=0}^{\infty} \frac{\psi_N(x_s,y_s,z_s)}{\Lambda_N[(k_N^2 - k^2) + j2kk_N\varsigma_N]} \tag{4.5}$$

$$\psi_N(x,y,z) = \cos\left(\frac{m\pi}{L_x}x\right)\cos\left(\frac{n\pi}{L_y}y\right)\cos\left(\frac{l\pi}{L_z}z\right) \tag{4.6}$$

$$k_N = \sqrt{\left(\frac{m\pi}{L_x}\right)^2 + \left(\frac{n\pi}{L_y}\right)^2 + \left(\frac{l\pi}{L_z}\right)^2} \tag{4.7}$$

$$\Lambda_N = \frac{1}{V}\int_V \psi_N \psi_M dV = \frac{1}{\epsilon_m \epsilon_n \epsilon_l} \qquad \epsilon_i = \begin{cases} 1, i = 0 \\ 2, i \neq 0 \end{cases} \tag{4.8}$$

where the subscript s refers to the source location, V is the volume of the room, Q is the volume velocity of the source, k is the wave number of the known source frequency ω, N is the number of room modes and ς_N is the damping constant, which was kept at a value of 0.01 for all frequencies and modes. The locations of the error sensors along with their respective objective function are given in Table 4-2.

Table 4-2: Sensor locations

Property	Location	Arena
Squared V_{comp}	(0.286m,0.432m)	Plate
Squared Velocity	(0.286m,0.432m)	Plate
Volume Velocity	(8 evenly spaced sensors in x, 12 evenly spaced sensors in y)	Plate
Acoustic Energy Density	(1.0m,1.0m, 1.0m)	Room

As a constraint of the gradient based algorithm, the control force was limited to five times the amplitude of the primary disturbance force.

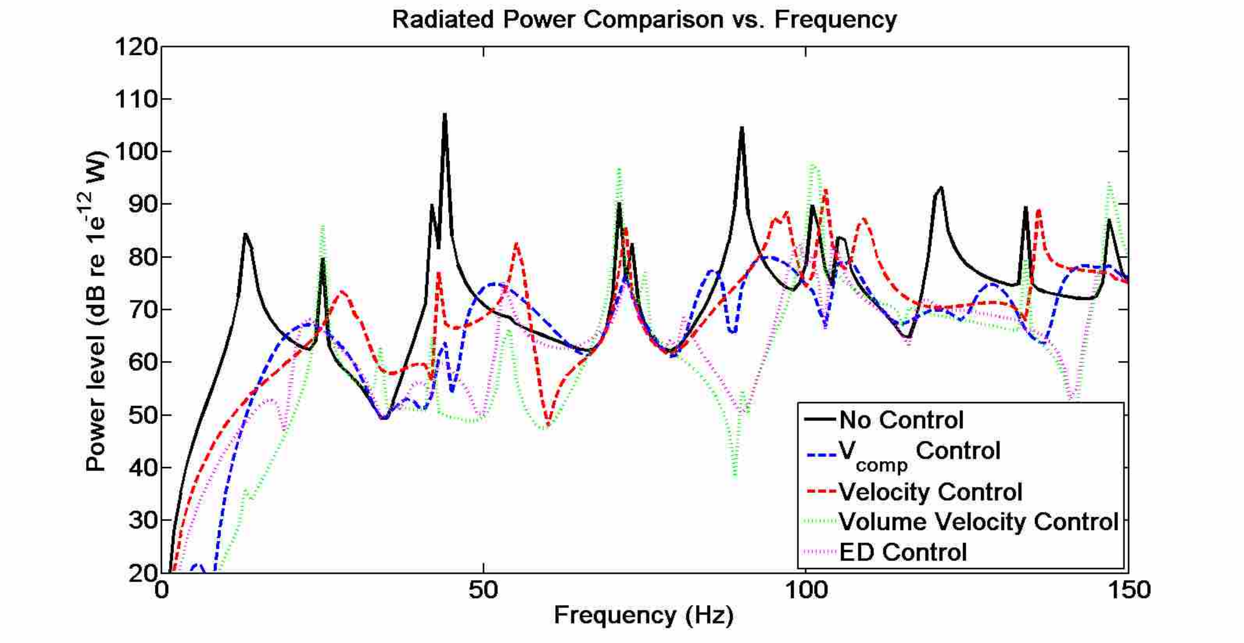

Figure 4-1: Objective function analytical radiated power comparison

The radiated power at frequencies spanning the first fifteen structural modes can be seen in Figure 4-1. Both the primary radiated power and the radiated power after implementing several control schemes are shown. The corresponding attenuations are given in Figure 4-2.

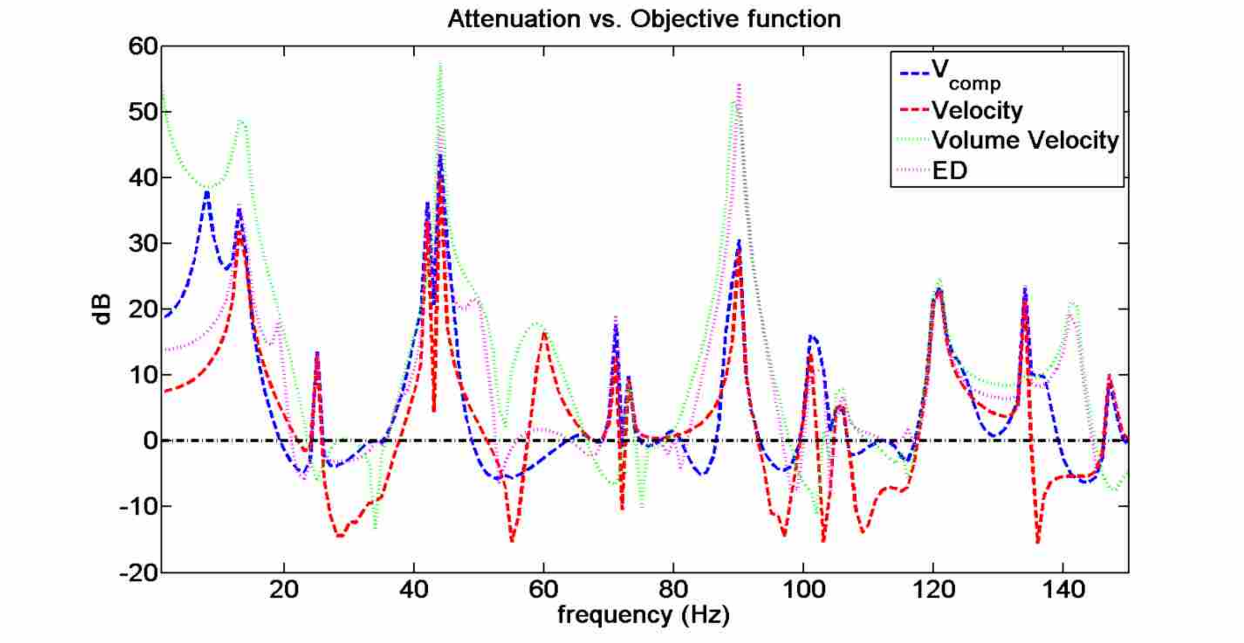

Figure 4-2: Objective function radiated power attenuation comparison

The average attenuation from each of the four cases is given in Table 4-3.

Table 4-3: Average attenuation vs. objective function

Control	Average Attenuation (dB)
Squared V_{comp}	5.8
Squared Velocity	2.7
Volume Velocity	12.4
Acoustic Energy Density	8.6

When comparing the overall attenuations, volume velocity does considerably better, but considering the number of sensors involved, it is less practical in implementation. Also, an important note is that the maximum increase in radiated power is less for squared V_{comp} control than for any other investigated control scheme. The maximum and minimum attenuations for each of the control cases are given in Table 4-4. The attenuation of the objective function values before and after control are given for reference in Figure 4-3 - Figure 4-6.

Table 4-4: Maximum and minimum attenuation vs. objective function

Control	Largest Attenuation (dB)	Largest Increase (dB)
Squared V_{comp}	43.5	6.3
Squared Velocity	40.0	15.6
Volume Velocity	57.5	13.5
Acoustic Energy Density	54.4	7.6

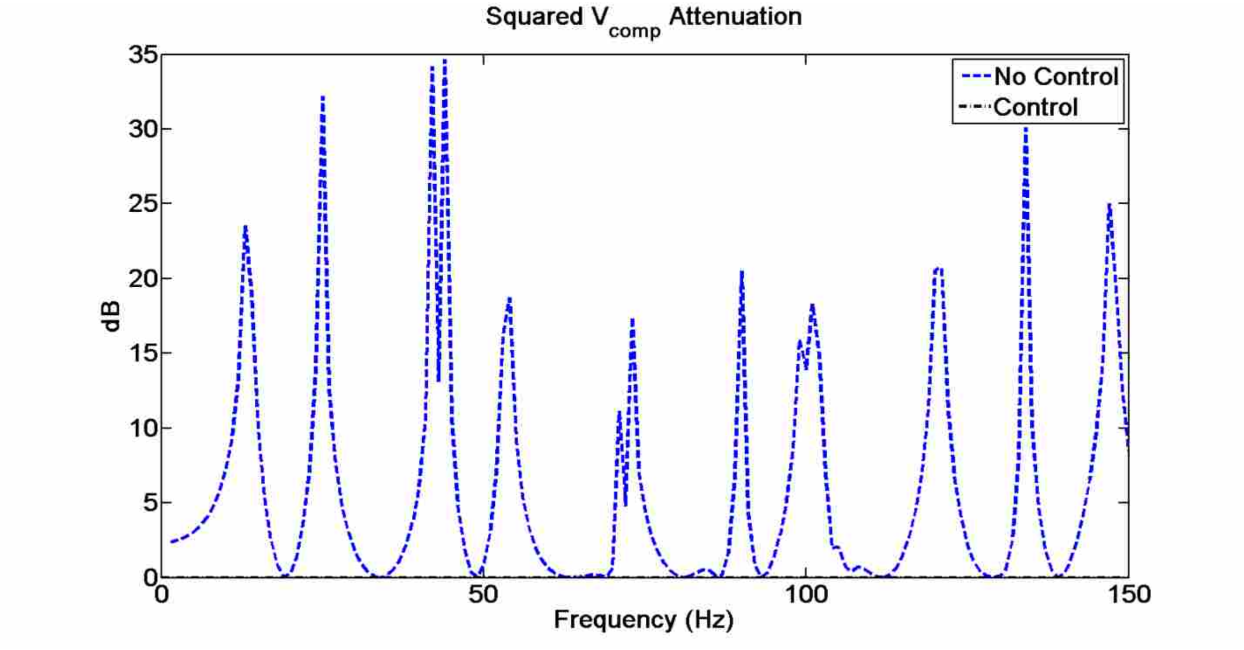

Figure 4-3: Squared V_{comp} at the measurement point before and after control

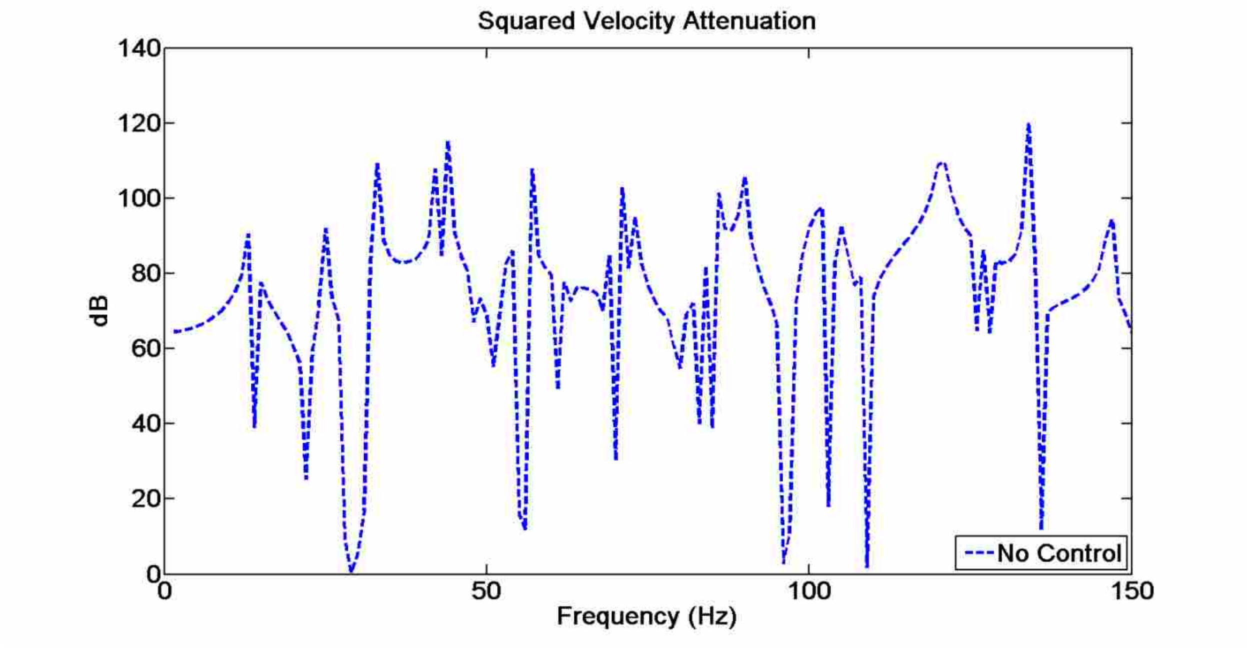

Figure 4-4: Velocity at the measurement point before and after control

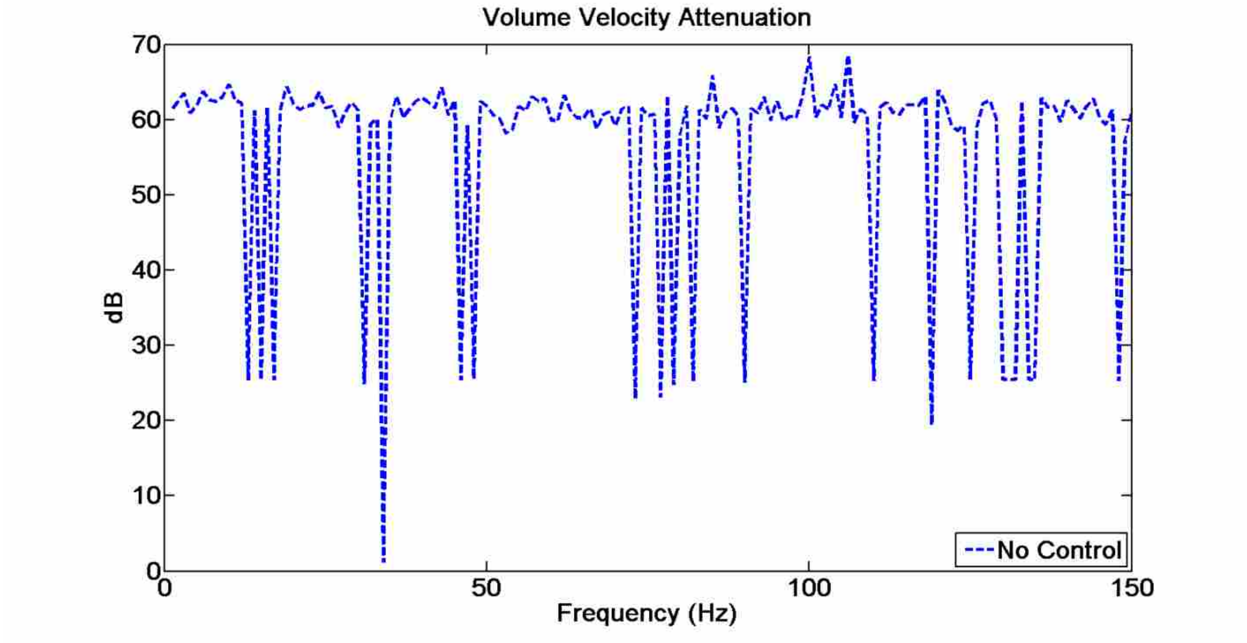

Figure 4-5: Volume velocity estimate using 96 sensors before and after control

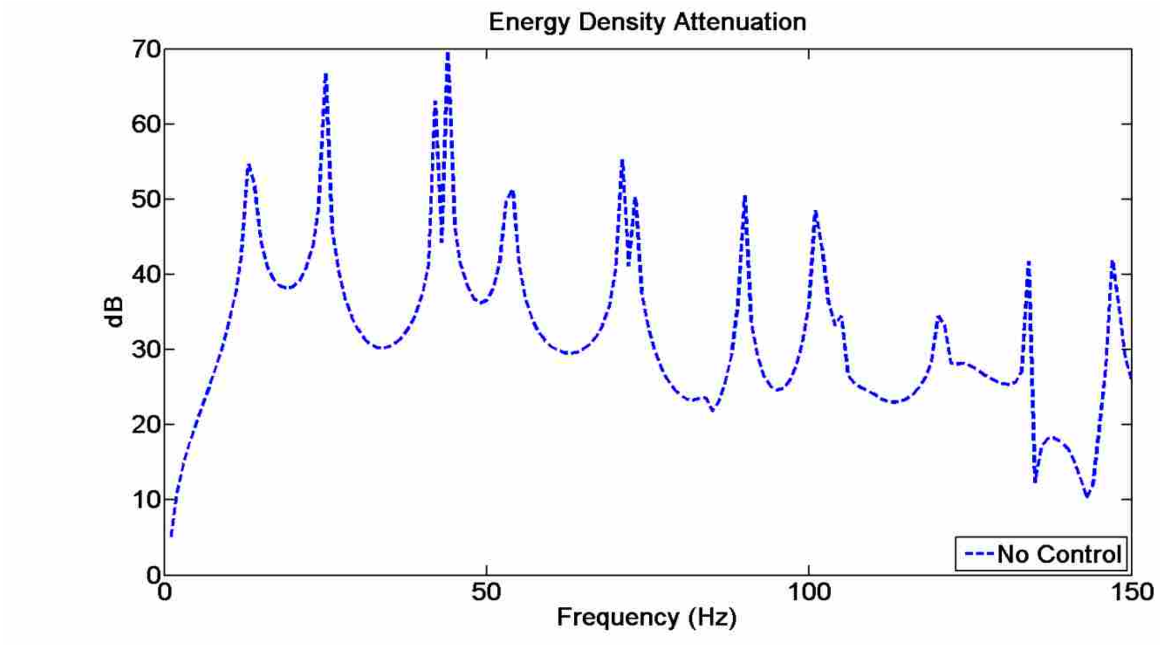

Figure 4-6: Energy density at the measurement point before and after control

Even though volume velocity control produced a larger overall attenuation, the maximum increase in radiated power is much more than when minimizing squared V_{comp} and again, uses considerably more measurement sensors, approximately fifteen times the amount needed for squared V_{comp}. In comparing squared V_{comp} control to acoustic energy density, which has been proven effective[6], squared V_{comp} attenuates the radiated power by a few decibel less overall, but considering the fact that sensors could be integrated into the structure and not cumbersomely placed in the sound field, the loss in control may be worth more efficient implementation, making it a beneficial structural objective function. As can be viewed in the results, controlling the quantity squared V_{comp} nearly always decreased the radiated power, attenuated all of the resonant peaks by at least 5 decibels and produced an overall reduction of almost six decibels. At some frequencies the radiated power was increased, but most frequencies saw a large reduction in radiated power and each of the resonance frequencies was attenuated significantly, except the (2,2) mode which corresponds to a frequency of 54Hz. Originally the (2,2) mode is a very inefficient radiating mode because of a zero volume velocity, but when modified during the control of squared V_{comp} it is restructured into a more efficiently radiating structure. However, it should be noted that this is due to a combined control actuator and objective function location rather than simply the objective function location. It was observed that a change in the control location in some instances lead to a decrease in the (2,2) mode radiated power as will be shown in section 4.3.

4.2 Sensor Placement

The measurement sensor for the previous case was placed in a location which would provide one of the best solutions in regards to velocity control. As shown in Figure 4-7, the sensor was placed at a location with no nodal lines, represented by the dashed lines, for the first fifteen structural modes.

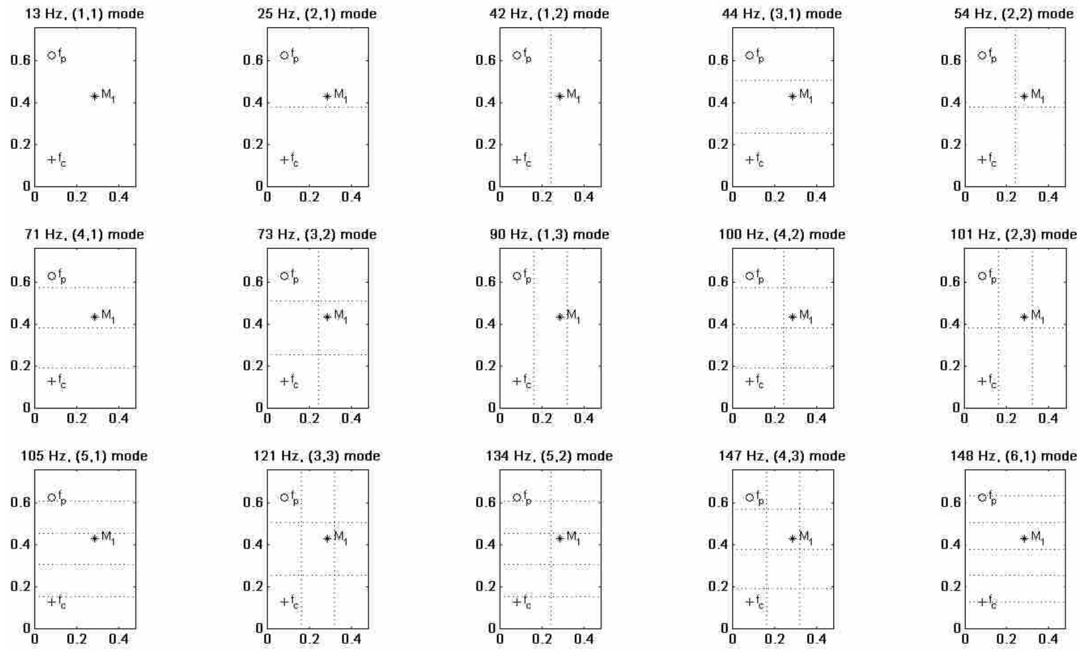

Figure 4-7: Sensor position vs. structural mode

Although the sensor was placed in this specific location to allow a point velocity objective function to have the best possible response, it does not allow V_{comp} to show its full potential. The largest benefit of controlling squared V_{comp} is that the control performance is largely independent of sensor location. To validate this, the sensor was moved to multiple locations on the plate and the experiment was repeated with comparable results at most all locations. Other plate locations are given in Figure 4-8 with the corresponding radiated power at each location given in Figure 4-9.

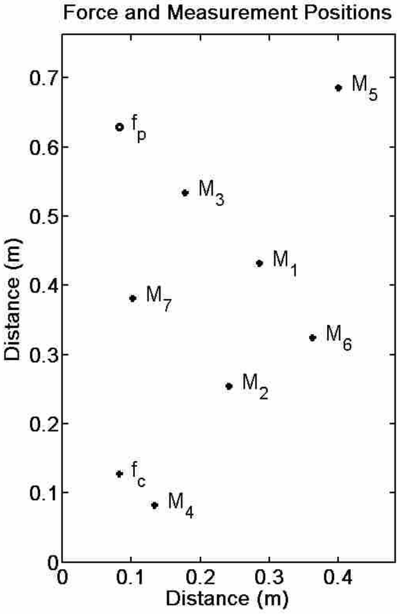

Figure 4-8: Force and sensor locations

In Figure 4-8 the primary force is denoted by f_p, the control force by f_c and the error sensor locations by M_1, M_2, M_3..., etc. It should be noted that the M_1 location is the location used previously. The radiated power can be seen in Figure 4-9 and the overall attenuation for each of the error sensor positions is given in Table 4-5.

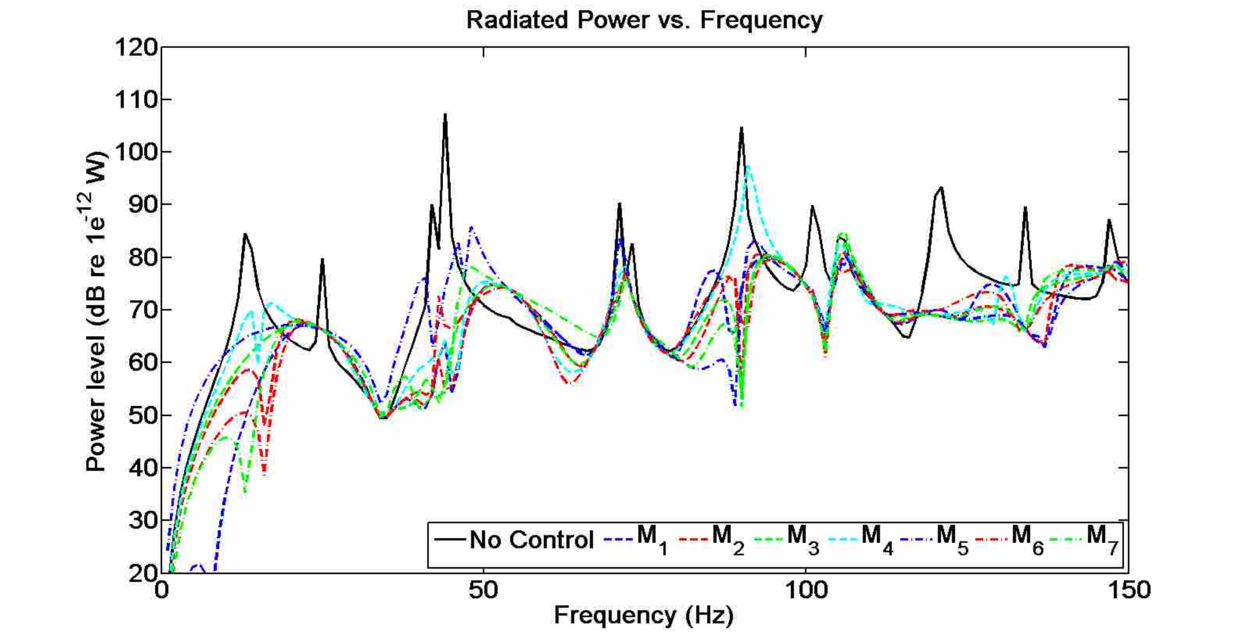

Figure 4-9: Analytical radiated power vs. sensor location

Table 4-5: Average attenuation using squared V_{comp} vs. measurement position

Measurement Position	*Average Attenuation (dB)*
M_1	5.8
M_2	4.6
M_3	4.2
M_4	2.5
M_5	2.4
M_6	4.9
M_7	4.8

As shown in Figure 4-9, locations M_1, M_2, M_3, M_6, and M_7 produced good results, while locations M_4 and M_5 produced an less desirable effect, leading to the notion that control is fairly independent of sensor location with the exception that error sensors should not be placed near the corners of the plate. This result is largely a function of using average values for α,β,γ and δ over the entire frequency range. If the actual optimal values for α,β,γ and δ are used for a specific mode, as is the case in Table 4-6, the overall attenuation is approximately equal, no matter the sensor placement. In this particular case, the plate was driven at the (3,3) mode and the corresponding values for α, β, γ and δ taken from Table 3-4 were used.

Table 4-6: Attenuation at the (3,3) using correct scaling values for squared V_{comp}

Measurement Position	*Attenuation at the (3,3) mode (dB)*
M_1	42.1
M_2	42.0
M_3	42.1
M_4	41.7
M_5	41.9
M_6	42.1
M_7	42.1

However, since an average α, β, γ and δ were selected; there are issues with placing sensors in corners. When placed in locations farther from the corners of the plate, the control of squared V_{comp} attenuated almost all of the peaks significantly and even provided control at frequencies other than the resonance frequencies. This result allows the sensor to be placed at a relatively arbitrary location, which placement requires no previous knowledge of the vibrating structure, making this technique exhibit a robustness in terms of sensor placement.

4.3 Control Actuator

An important part of an active noise control or vibration control system is the placement of the control actuator and the amount of power it has to exert in order to cancel the proposed objective function. A comparison of magnitude and phase of the control force against each of the objective functions is given in Figure 4-10 and Figure 4-11, respectively. The sensors were kept in the same locations discussed previously and are shown in Table 4-2.

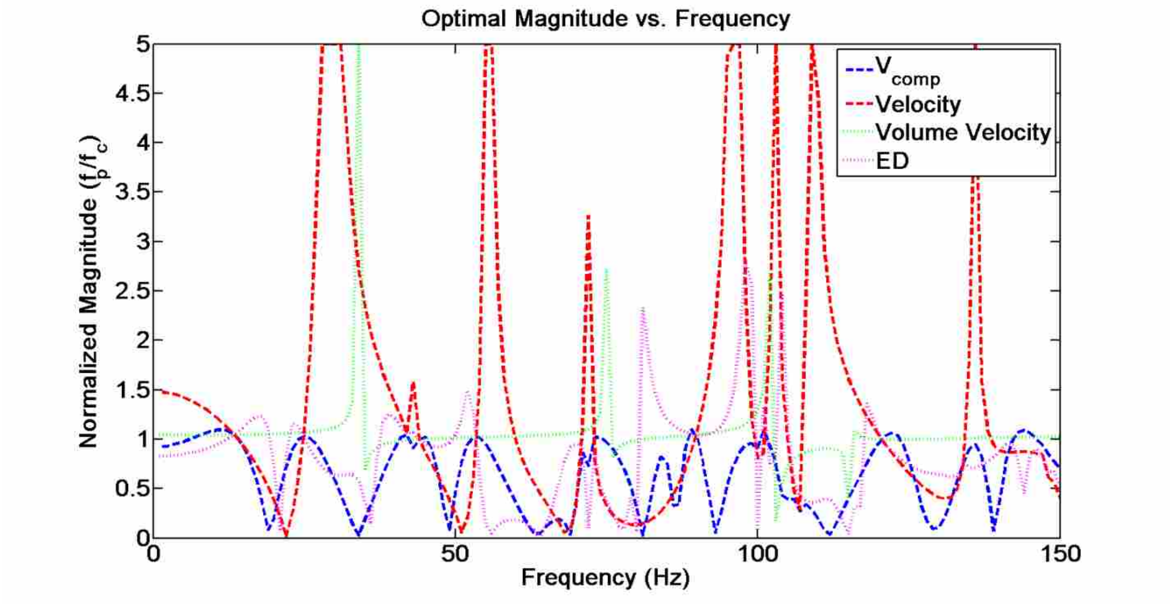

Figure 4-10: Control force magnitude vs. objective function

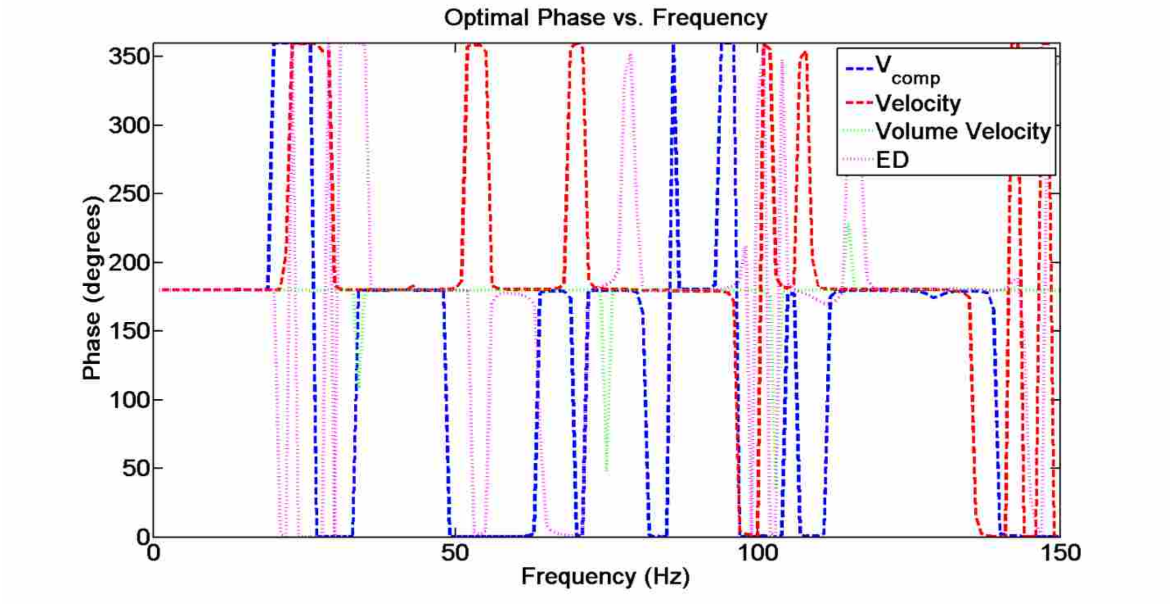

Figure 4-11: Control force phase vs. objective function

It can be noted that the controller would have become unstable, possibly driving the control force output to infinity if a cap of five times the input magnitude was not placed on the control output magnitude. This mainly happened with the point velocity control, although it did occur in one instance with volume velocity control. When squared V_{comp} was chosen as the objective function, the control output varied from zero to a little over the primary force amplitude, while all the other objective functions at one point or another required a larger power output from the control force. This shows that the objective function, squared V_{comp}, produces desirable results and does so with less power required for the controller than the other objective functions.

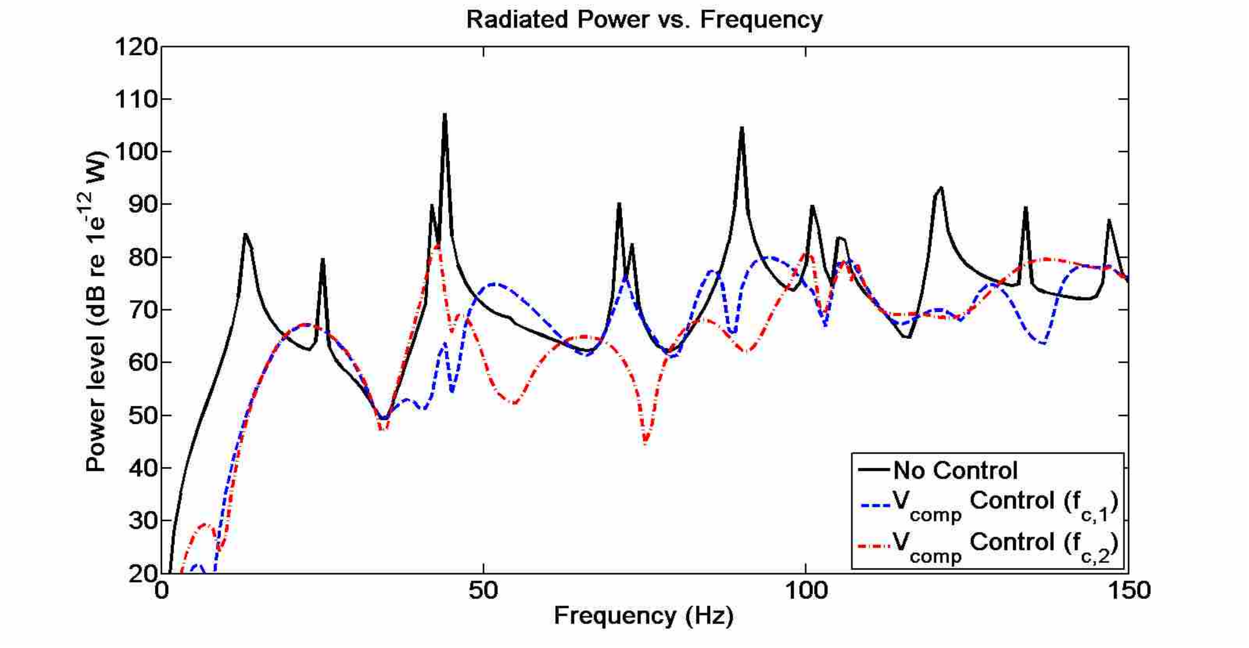

Figure 4-12: Radiated power comparison between control force locations

As mentioned earlier, although the sensor can be moved around without much change in the performance, the placement of the control force does affect the overall performance of the system and will produce different results. Keeping the same primary force location and sensor locations, the control force was moved to (0.406m, 0.127m). The results, compared to the original setup, are given in Figure 4-12 and the average attenuation over the frequency band shown is given in Table 4-7.

Table 4-7: Average attenuation vs. control location

Control Force Position	*Attenuation at the (3,3) mode (dB)*
$F_{c,1}$	5.8
$F_{c,2}$	6.6

The control location does have a large effect on the overall system performance. When comparing the two cases, it can be seen that the second control location provided an attenuation at the (2,2) mode, 54Hz, while the original control location boosted the power. However, at other modes, the first control location proves better as is the case with the (5,2) mode, 134Hz. A more thorough investigation of the optimal control force location is needed in general but will not be completed in this thesis.

4.4 Radiation Mode Comparison

A reason for the success of squared V_{comp} at certain modes and the lack of success of volume velocity is associated with the concept of acoustic radiation modes. As shown by Sors and Elliott[2], volume velocity is a strong measure of the first acoustic radiation mode. When the first radiation mode has a strong response relative to the others, volume velocity control will perform well. The success of this new method lies in V_{comp}'s ability to control a larger number of acoustic radiation modes, as its terms mimic radiation mode shapes. A comparison of the power radiated by each radiation mode, as given by Eq. 3.8, is shown in Figure 4-13 - Figure 4-16.

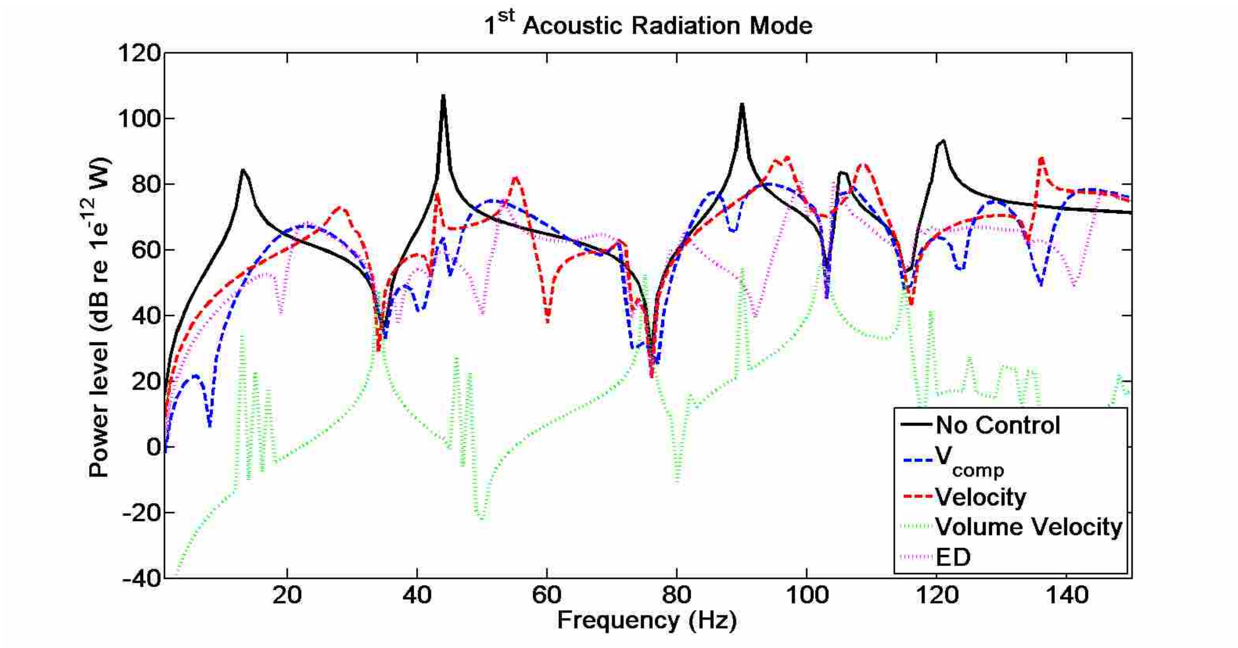

Figure 4-13: Power radiated by the first acoustic radiation mode

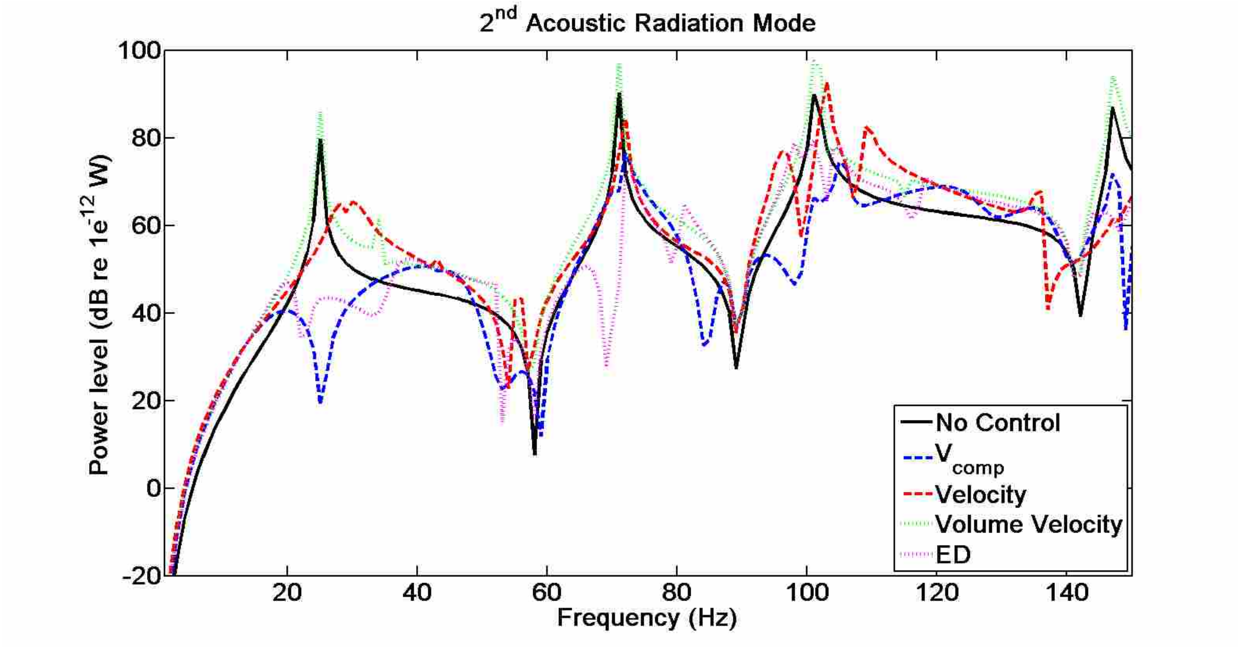

Figure 4-14: Power radiated by the second acoustic radiation mode

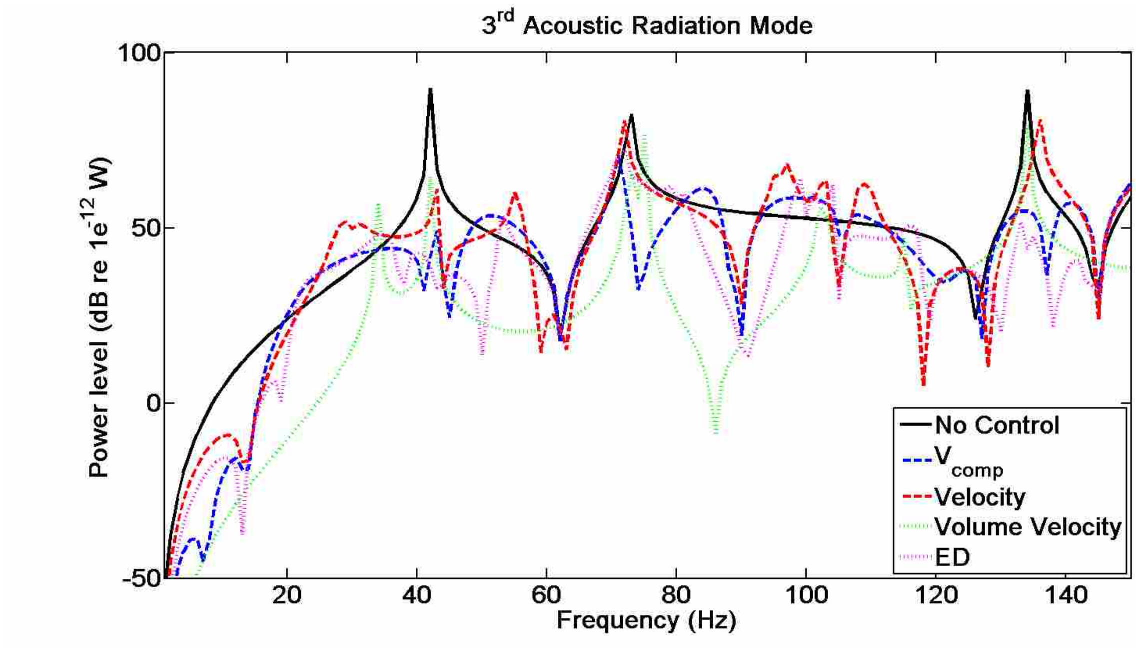

Figure 4-15: Power radiated by the third acoustic radiation mode

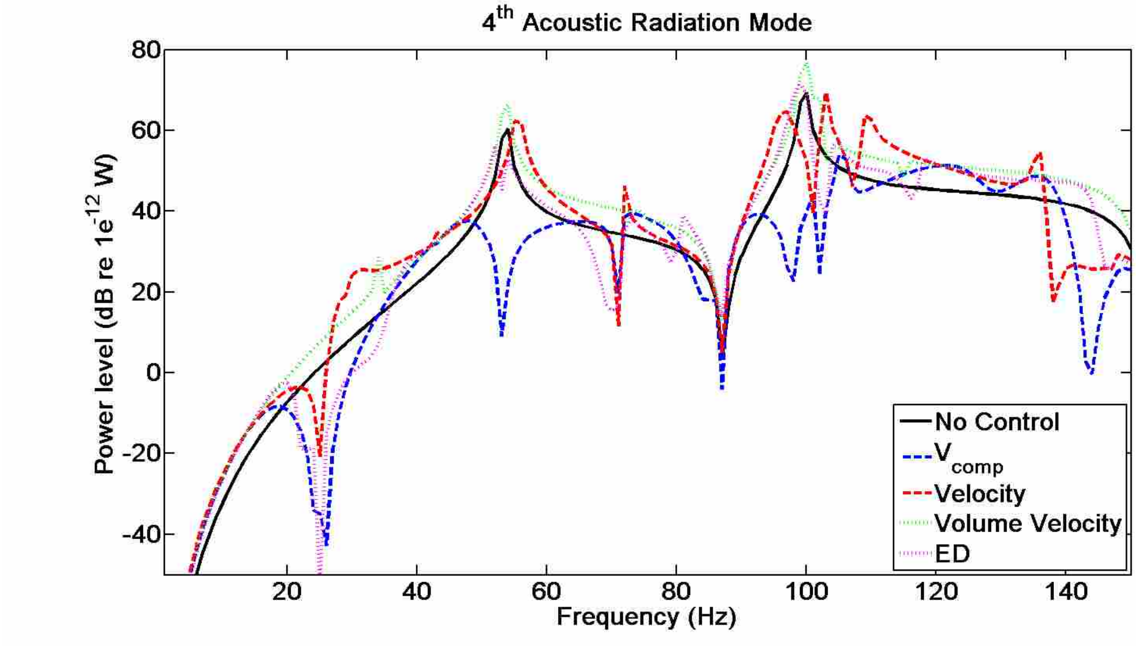

Figure 4-16: Power radiated by the fourth acoustic radiation mode

In comparing all of the cases, squared V_{comp} was the only control case which attenuated all of the peaks of the first four acoustic radiation modes. Energy density came close, but failed to control one of the peaks of the fourth radiation mode which corresponds to a frequency of 100Hz as can be seen in Figure 4-16. Although volume velocity preformed well overall, it did not attenuate any of the peaks for the even radiation modes as shown in Figure 4-14 and Figure 4-16. Squared V_{comp}, as a structural control metric, performs well in a broadband system because of its ability to control acoustic radiation modes.

5 EXPERIMENTAL SETUP

This chapter explains the experimental method used to investigate the effects of squared V_{comp} control on the acoustic field.

5.1 Measurement Array

Because the spatial derivatives are only first and second order, a simple four transducer array can be used to acquire all the terms in squared V_{comp}. The positioning of this array is shown in Figure 5-1.

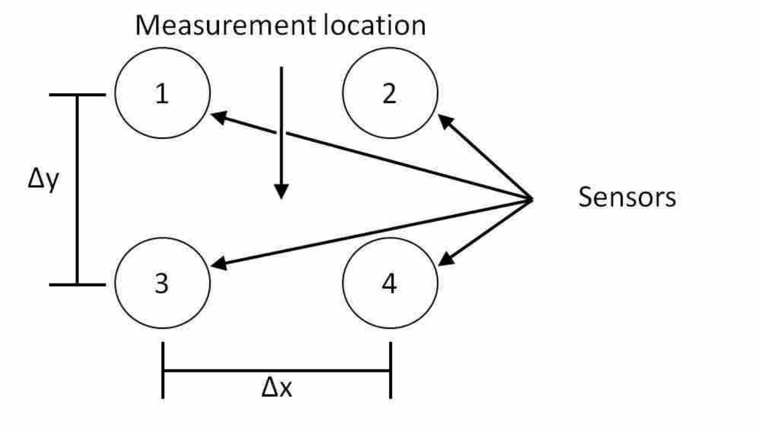

Figure 5-1: Squared V_{comp} sensor configuration

Using accelerometers, equations for all four terms making up squared V_{comp} using finite differencing are given as

$$\frac{dw}{dt} = \int \frac{a_1 + a_2 + a_3 + a_4}{4} dt \tag{5.1}$$

$$\frac{d^2w}{dxdt} = \int \frac{1}{2\Delta x} (a_2 + a_4 - a_1 - a_3) dt \tag{5.2}$$

$$\frac{d^2w}{dydt} = \int \frac{1}{2\Delta y} (a_1 + a_2 - a_3 - a_4) dt \tag{5.3}$$

$$\frac{d^2w}{dxdydt} = \int \frac{1}{\Delta x \Delta y} (a_2 - a_1 - a_4 + a_3) dt \tag{5.4}$$

The sensor spacing used in the remainder of the thesis is 0.0254m in both the x and y directions. This particular spacing was chosen due to the frequency band of interest. The phase differences, in degrees, with this spacing for the frequency range of interest are given in Table 5-1 with the equation used given by

$$\emptyset = \frac{\Delta}{\lambda_s} * 360^{\mathrm{o}} \tag{5.5}$$

where λs is the longest structural wavelength at the driving frequency and Δ is the accelerometer spacing in the direction of the longest structural wavelength. These phase differences are large enough so as to minimize noise floor issues as well as to overcome any small phase mismatch errors in the accelerometers which in this case were much smaller than a degree.

Table 5-1: Maximum and minimum phase between accelerometers

Phase at 30Hz	*Phase at 175Hz*
Approx 6°	Approx. 36°

5.2 Update for the FXLMS Algorithm

In order to implement the control experimentally, a previously developed acoustic energy density control code employing the filtered-x least mean squared (FXLMS) algorithm was modified to minimize squared V_{comp}. The FXLMS algorithm has proved useful in many active control situations[4] and is the dominant algorithm used in active control systems reported in the literature. The development of an energy-based control law for the FXLMS algorithm was set forth by Sommerfeldt and Nashif[7], and the following development of the squared V_{comp} control update was based on this work. The performance function V_{comp}, as given in section 3.3 but shown again for reference, is given by

$$\left(V_{comp}\right)^2 = \alpha\left(\frac{dw}{dt}\right)^2 + \beta\left(\frac{d^2w}{dxdt}\right)^2 + \gamma\left(\frac{d^2w}{dydt}\right)^2 + \delta\left(\frac{d^3w}{dxdydt}\right)^2 \tag{5.6}$$

where α, β, γ, and δ are scaling factors solved for a priori, $\frac{dw}{dt}$ is the transverse velocity, $\frac{d^2w}{dxdt}$ is a rocking of the velocity in the x-direction, $\frac{d^2w}{dydt}$ a rocking in the y-direction, and $\frac{d^3w}{dxdydt}$ is the twist in the velocity all measured at a single location.

A filtered-x control implementation for this case can be represented in block diagram form as shown in Figure 5-2. In this figure the subscript p refers to the velocities at the error sensor in the absence of the control, and the subscript c refers to these velocities due to the control. It should also be noted that t refers to a discrete-time index. W(z) represents the transfer function of the control filter, and $H_{\dot{w}}(z)$, $H_{\dot{w}x}(z)$, $H_{\dot{w}y}(z)$, and $H_{\dot{w}xy}(z)$ represent the transfer function between the control output and the components measured by the error sensor with XXX signifying the time derivative of the displacement. $L\{\dot{w}, \dot{w}_x, \dot{w}_y, \dot{w}_{xy}\}$ represents any extra processing of the error signals which is required to obtain the "effective" error signal. In the case of squared V$_{comp}$, this would result in the scaling of the individual terms by the previously solved α, β, γ, and δ.

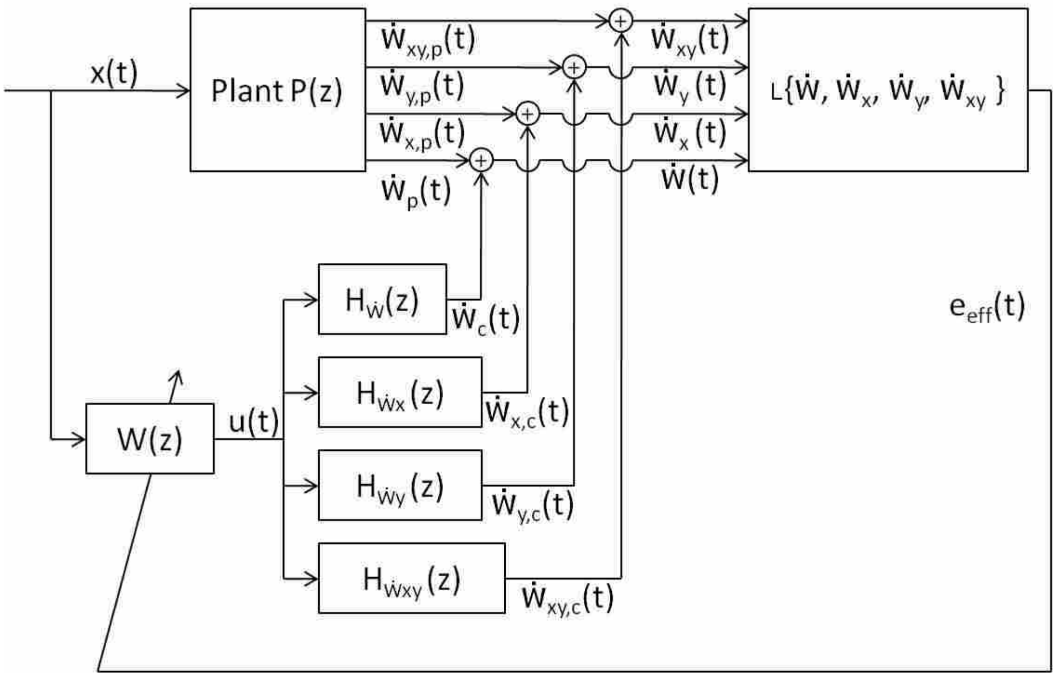

Figure 5-2: Block diagram representation of a filtered-x control implementation for controlling the structural quantity squared V$_{comp}$

Based on the energy control update by Sommerfeldt and Nashif[6], the objective function, chosen to be squared V$_{comp}$, can be expressed as

$$\begin{aligned} J_{V_{comp}{}^2} = {} & \alpha\left(\frac{dw}{dt}_p + W^T R_{dw/dt}\right)^2 + \beta\left(\frac{d^2w}{dxdt_p} + W^T R_{d^2w/dxdt}\right)^2 \\ & + \gamma\left(\frac{d^2w}{dydt_p} + W^T R_{d^2w/dydt}\right)^2 \\ & + \delta\left(\frac{d^2w}{dxdydt_p} + W^T R_{d^2w/dxdydt}\right)^2 \end{aligned} \tag{5.7}$$

The gradient of the performance function is required to update the control coefficients and is given in Eq. 5.8.

$$\nabla J_{V_{comp^2}} = 2\alpha\left(\frac{dw}{dt}_p + W^T R_{dw/dt}\right) R_{dw/dt} + 2\beta\left(\frac{d^2w}{dxdt_p} + W^T R_{d^2w/dxdt}\right) R_{d^2w/dxdt}$$
$$+ 2\gamma\left(\frac{d^2w}{dydt_p} + W^T R_{d^2w/dydt}\right) R_{d^2w/dydt} \tag{5.8}$$
$$+ 2\delta\left(\frac{d^2w}{dxdydt_p} + W^T R_{d^2w/dxdydt}\right) R_{d^2w/dxdydt}$$

This subsequently leads to the control law implementation expressed as

$$W(t+1) = W(t)$$
$$- \mu\left[2\alpha \frac{dw}{dt}_m (t)\ R_{dw/dt}(t) + 2\beta \frac{d^2w}{dxdt_m} (t)\ R_{d^2w/dxdt}(t)\right. \tag{5.9}$$
$$\left. + 2\gamma \frac{d^2w}{dydt_m} (t)\ R_{d^2w/dydt}(t) + 2\delta \frac{d^2w}{dxdydt_m} (t)\ R_{d^2w/dxdydt}(t)\right]$$

Using the four transducer array as given previously, gives the following approximations in terms of a finite differencing scheme

$$\frac{dw}{dt}_m = \frac{dw}{dt}_p + W^T R_{dw/dt} = \int \frac{a_1 + a_2 + a_3 + a_4}{4} dt \tag{5.10}$$

$$\frac{d^2w}{dxdt_m} = \frac{d^2w}{dxdt_p} + W^T R_{d^2w/dxdt} = \int \frac{1}{2\Delta x}(a_2 + a_4 - a_1 - a_3)dt \tag{5.11}$$

$$\frac{d^2w}{dydt_m} = \frac{d^2w}{dydt_p} + W^T R_{d^2w/dydt} = \int \frac{1}{2\Delta y}(a_1 + a_2 - a_3 - a_4)dt \tag{5.12}$$

$$\frac{d^2w}{dxdydt_m} = \frac{d^2w}{dxdydt_p} + W^T R_{d^2w/dxdydt} = \int \frac{1}{\Delta x \Delta y}(a_2 - a_1 - a_4 + a_3)dt \tag{5.13}$$

where m signifies the measured signal. Because the experimental plate will be excited at a single frequency at one particular time, the integral in Eqs. 5.10-5.13 is not necessary. With a known driving frequency, the scaling factor to compute a velocity given an acceleration is a constant, iω. Because each of the four terms given in Eqs. 5.10-5.13 are all approximated using acceleration signals, each would need to be multiplied by the same constant to compute the velocities and for this reason acceleration signals will give the same result as if velocities were used.

5.3 Experimental Setup

A steel clamped plate of dimensions 0.438 m x 0.762 m x 0.001 m was installed in between a large and a small reverberation chamber, with approximate resonance frequencies given in Table 5-2. The resonance frequencies were acquired using a scanning laser Doppler vibrometer (SLDV) with a resolution of 0.325Hz. The setup can be seen in Figure 5-3.

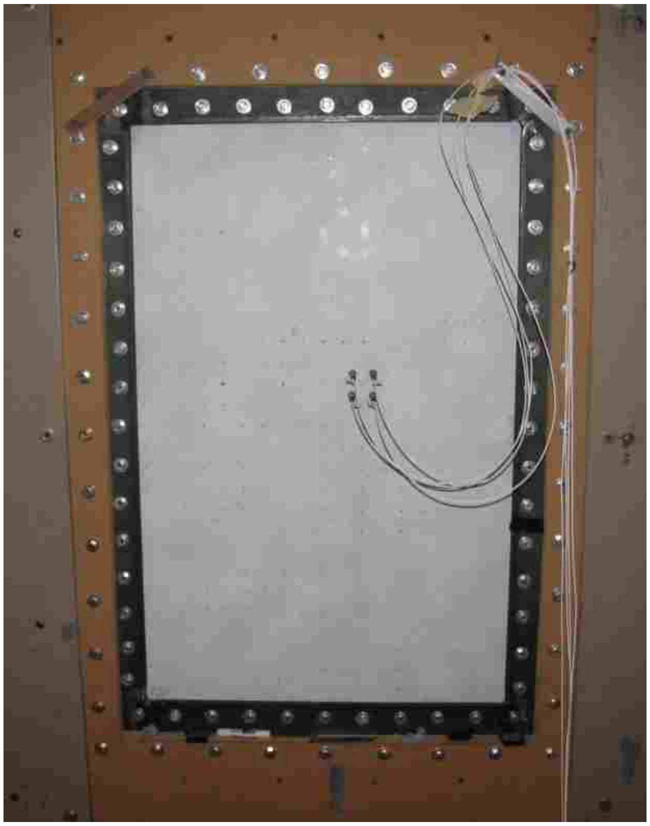

Figure 5-3: Picture of the experimental plate setup

The large and small chambers have dimensions 4.96m X 5.89m X 6.98m and 5.70m X 2.50m X 4.30m, respectively. Electrodynamic actuators were used for both the primary and control forces and were mounted to the plate in the large chamber. Eleven randomly distributed microphones were placed in the small chamber to measure the level of attenuation between the controlled and uncontrolled case. As the frequencies investigated are below the Schroder frequency of the small chamber, given at 552 Hz[18], the field could not be considered diffuse and therefore an accurate estimate of the potential energy in the room could not be acquired. However, using the eleven microphones, the measure of the attenuation in the room was determined to be accurate within 0.1 dB. Using four separate microphone distributions, a speaker was excited at a given voltage and then doubled. Each of the four microphone distributions were compared against each other and although the potential energy estimate varied significantly, in some cases almost double, the attenuation in all of the cases was accurate to within 0.1 dB. This procedure was completed at four different frequencies spanning the frequency range of interest, 30-180Hz.

Table 5-2: Resonance frequencies of the experimental plate

Mode	*Modal frequency Hz*
(1,1)	30.6
(2,1)	43.4
(3,1)	65.6
(1,2)	67.8
(2,2)	79.3
(4,1)	92.8
(3,2)	99.3
(4,2)	129.0
(3,3)	148.3
(5,2)	163.1
(4,3)	173.7

As can be seen, the analytical and experimental plates differ in a number of respects. First, the boundary conditions are not the same. The analytical solution was based on a simply supported plate while the experimental setup has an approximately clamped boundary condition. Second, the resonance frequencies show some differences with the resonance frequencies of the experimental setup given in Table 5-2. For example, the (1,3) mode does not exhibit itself in the experimental setup and the (3,1) mode presents itself at a frequency below the (1,2) mode contrary to what was seen in the analytical model. Modifications could have been made to the analytical model to create a better match, but as the purpose was to show general trends, no modifications were completed.

Because of the differences between the analytical and experimental setups, a more realistic α, β, γ, and δ for the experimental setup was determined. The values were determined by scanning the plate with the SLDV at each mode, computing the values of α,β,γ, and δ, and then averaging them over all modes. The scaling values used in the control code are given in Table 5-3.

Table 5-3: Squared V_{comp} scaling values used in the experimental case

α	β	γ	δ
1.0	0.005	0.007	0.00005

Four accelerometers were attached to the plate at the location used in the analytical setup and in the same fashion as given in Figure 5-1. The control system implemented in this particular case was developed previously by Faber and Sommerfeldt[17] and used acoustic energy density as the objective function. The same system was used for this particular case with the exception that the update equation was modified to use squared V_{comp} as the objective function. A program, ANC Remote, also developed by Faber, was used as an interface between the PC and the DSP. The results obtained from controlling squared V_{comp} using the aforementioned update equation will now be presented.

5.4 Experimental Results

As the frequencies of interest lie below 200Hz, only the acoustic attenuation could properly be determined as explained in section 5.3. Both squared V_{comp} and squared velocity were used as objective functions, and their respective attenuations of the acoustic field are given in Figure 5-4.

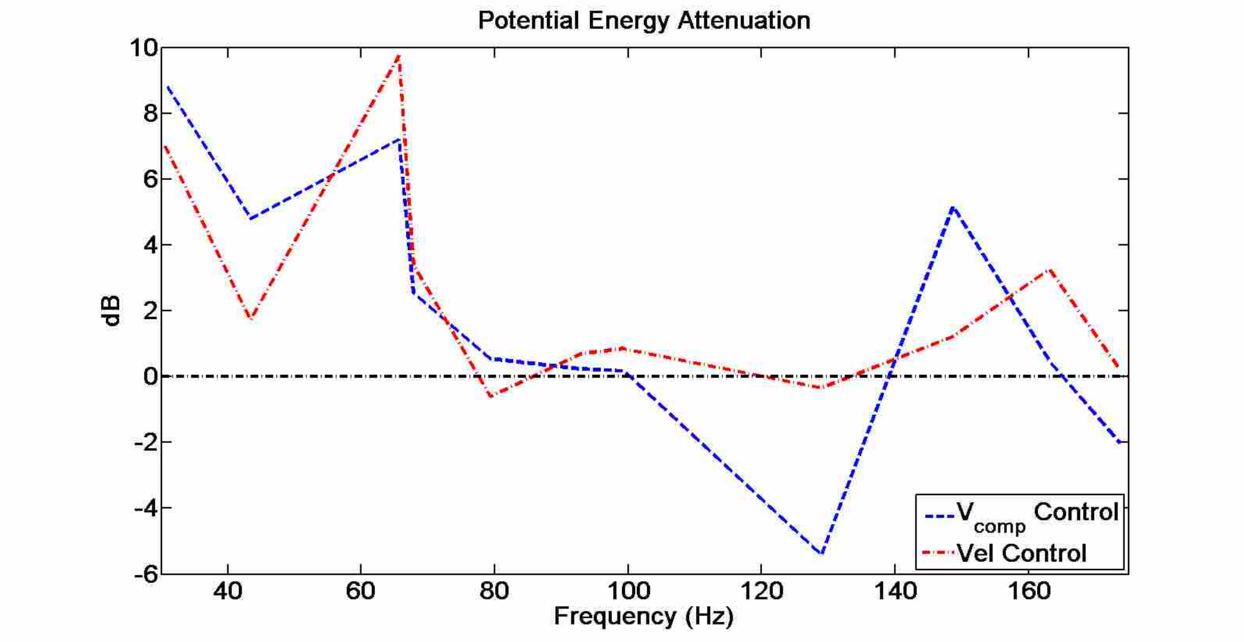

Figure 5-4: Experimental potential energy attenuation

Unfortunately, the results do not completely follow the trends set forth by the analytical solution. In some cases, a point velocity measurement objective function proved more beneficial than the control of squared V_{comp}, at least when looking at attenuation. However, after looking more closely, it was noticed that when the control of squared V_{comp} produced poor results it was due to a poor convergence of the controller. For two of the frequencies, 129.0Hz and 173.7Hz, the controller did not converge to a solution, so the algorithm was terminated at a point and the measurements were taken. At many frequencies, squared V_{comp} was either not attenuated significantly or was increased, again alluding to the fact that the controller did not converge correctly. The squared velocity attenuation is given in Figure 5-5 showing that velocity at every frequency of interest was attenuated significantly. Squared V_{comp} attenuation is given in Figure 5-6

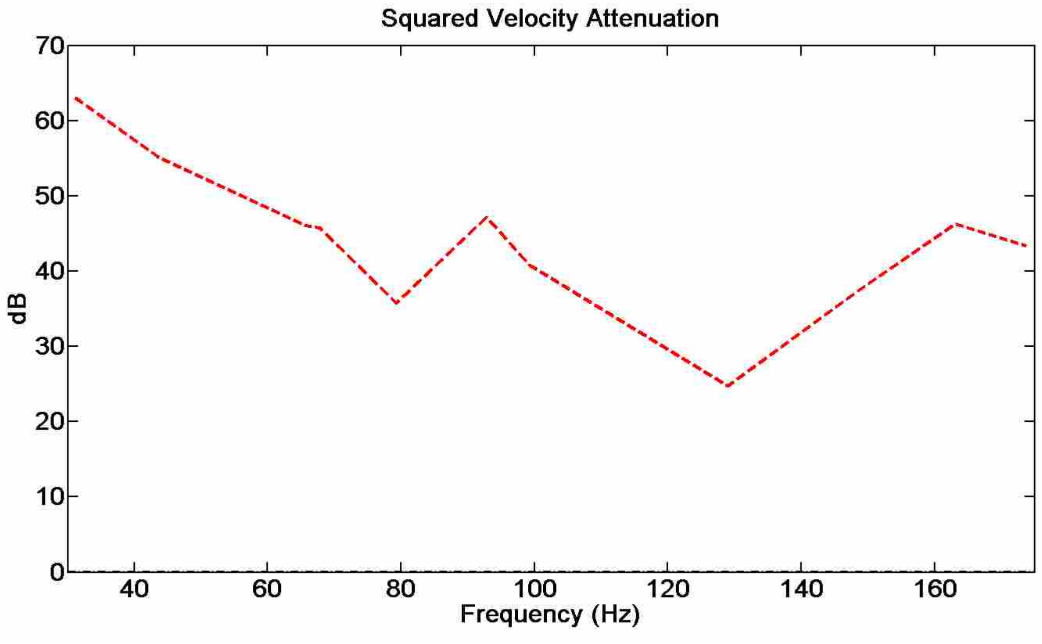

Figure 5-5: Experimental Squared velocity attenuation before and after control

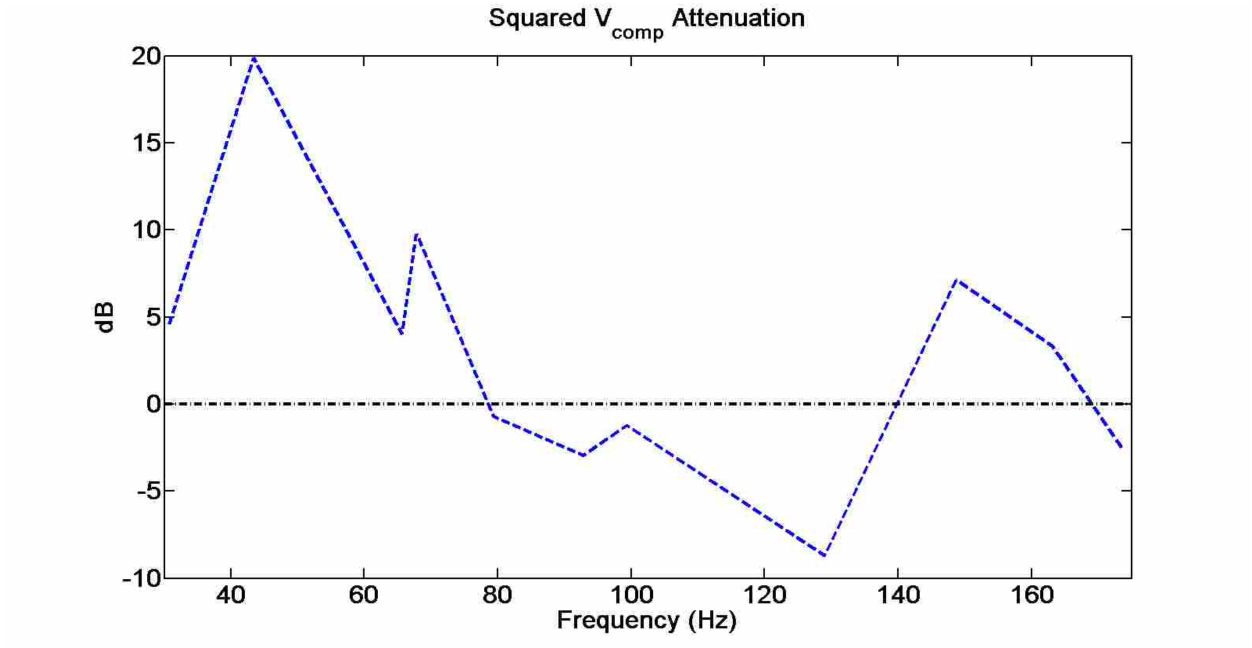

Figure 5-6: Experimental squared V_{comp} attenuation

When comparing Figure 5-4 and Figure 5-6, the potential energy was attenuated when V_{comp} was also attenuated. At most frequencies, squared V_{comp} was not able to be attenuated by more than 5-10 dB, suggesting that the control algorithm was not able to converge completely or that it reached a point where it could no longer attenuate the objective function.

Frequencies of 43.4 Hz and 129.0 Hz will provide useful insight as they end up on different ends of the spectrum in terms of control. When using the program ANC Remote to interface with the DSP, real time data can be viewed through separate windows. Screenshots of ANC Remote will be shown here to illustrate why the controller would not converge in many instances. Figure 5-7 gives the gradients of each of the four terms of squared V_{comp} as seen by the controller. It should be noted that the red dashed line represents zero voltage.

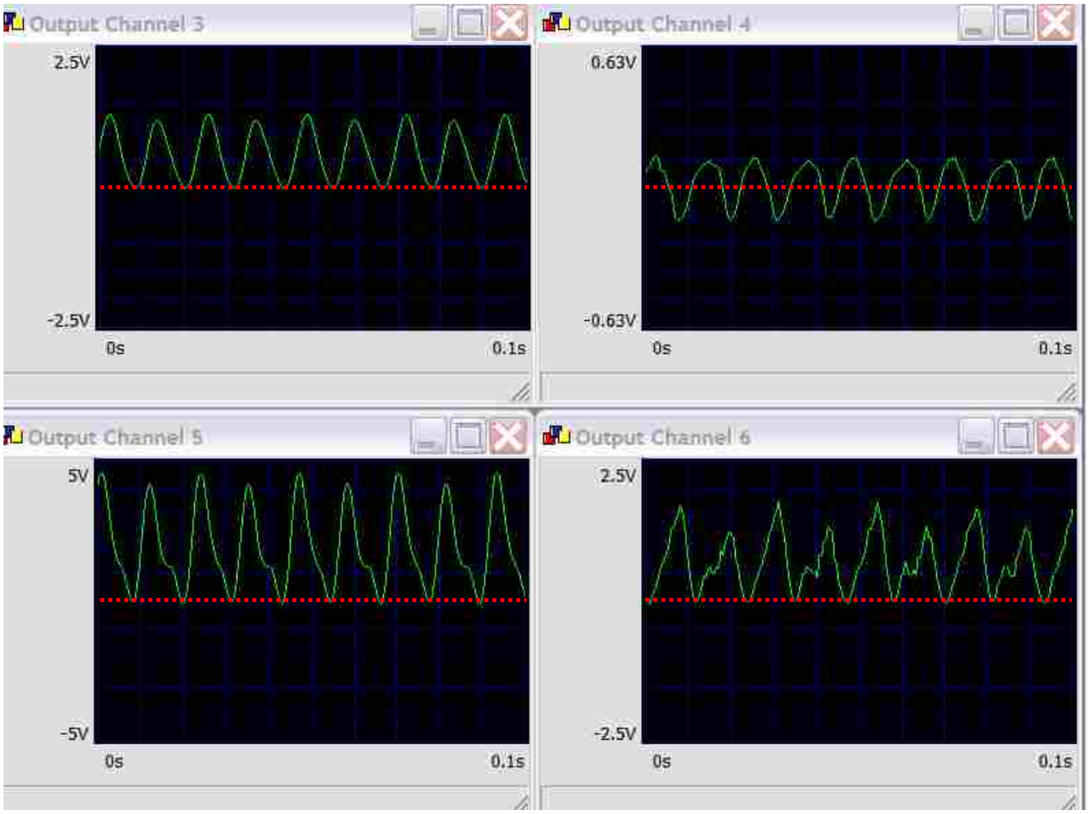

Figure 5-7: Time history of individual gradient terms at the (2,1) mode (25Hz) before control

Output channel 3 gives a time history of the transverse velocity gradient taken from Eq. 5.8.

$$Output\ Channel\ 3 = 2\alpha\left(\frac{dw}{dt}_p + W^T R_{dw/dt}\right) R_{dw/dt} \tag{5.14}$$

Channel 4 gives the x derivative gradient, channel 5 gives the y derivative and finally channel 6 gives the twisting term derivative. Dissecting Eq. 5.14 shows two main components: first is the actual measured error signal denoted by

$$\frac{dw}{dt}_p + W^T R_{dw/dt} \tag{5.15}$$

and the second is the filtered-x signal given by

$$R_{dw/dt} \tag{5.16}$$

The R term is obtained using the estimated transfer function $H_{\dot{w}}$ and the filtered-x signal. To visualize the process, both of these terms can be looked at as cosine terms. When a cosine function is squared, it creates a signal oscillating at twice the frequency as the original along with a DC offset or bias. This DC offset will be maximized if the cosine functions are completely in phase with each other, or completely correlated. If there is a portion which is uncorrelated, the DC offset, or mean, will shift toward zero.

Observing Figure 5-7, most all of the terms are correlated or at least have a strong correlation. The sum of these gradients, as given by Eq. 5.8. can be seen in Figure 5-8. Note the positive DC offset apparent in this response. It should also be noted that this is before the control is activated. Once the controller is allowed to converge, the final gradients can be seen in Figure 5-9.

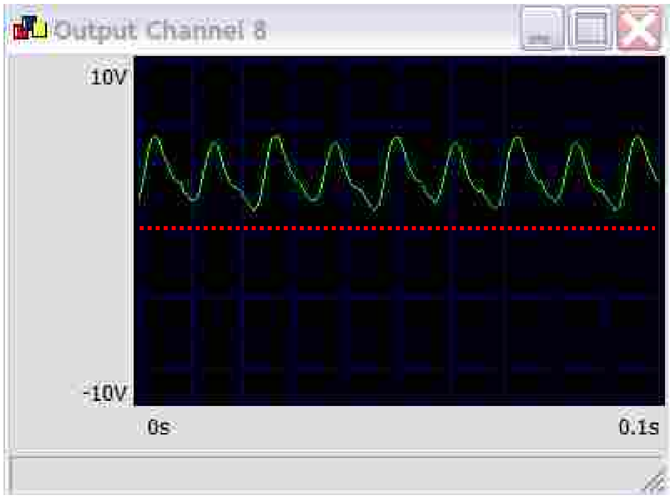

Figure 5-8: Time history of the gradient used to update the control filter for the (2,1) mode before control

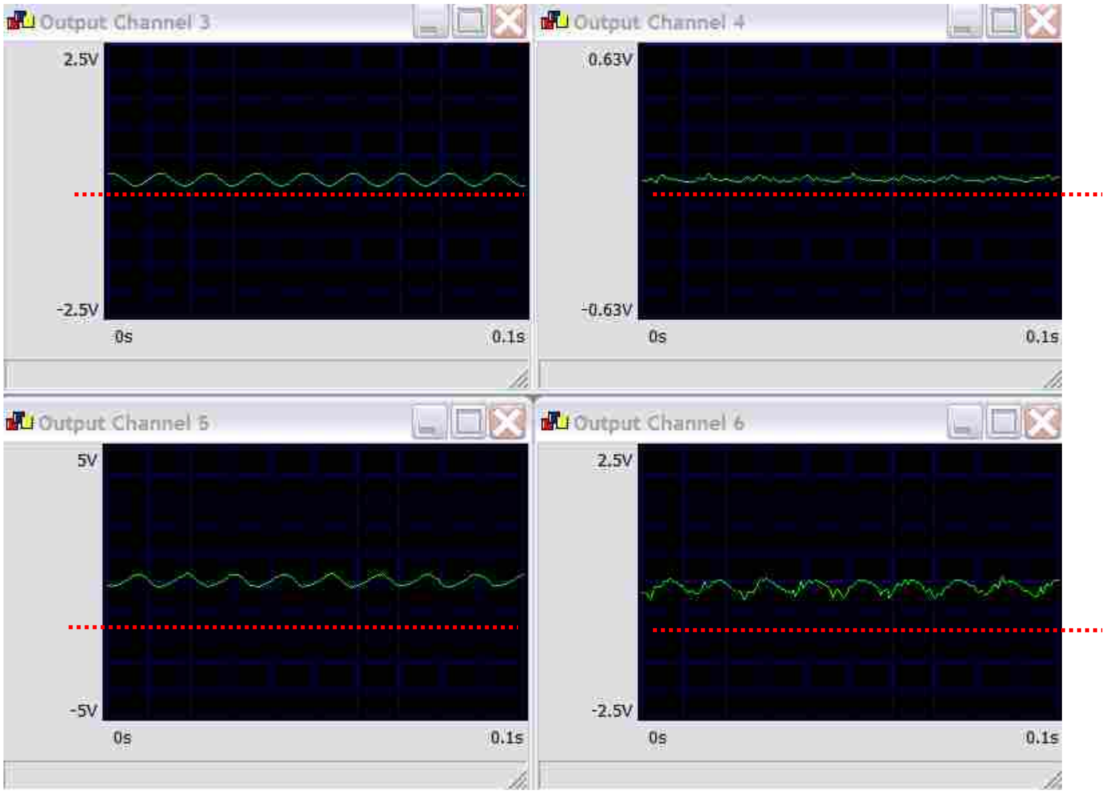

Figure 5-9: Time history of individual gradient terms at the (2,1) mode after control

The DC offset associated with each of the terms has been shifted to zero and the amplitudes are also attenuated, with the complete gradient shown in Figure 5-10.

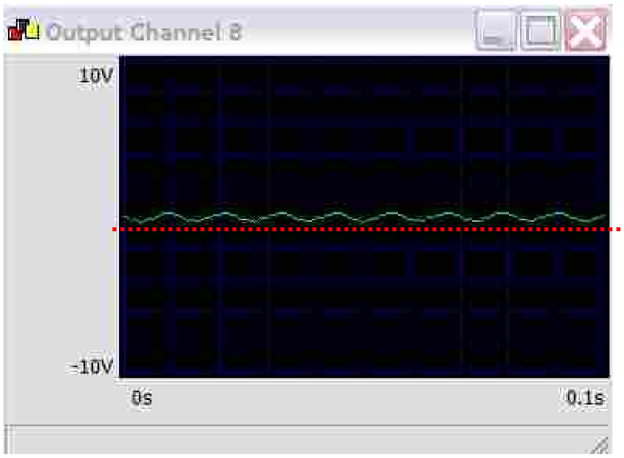

Figure 5-10: Time history of the gradient used to update W for the (2,1) mode after control

When comparing a case which did not perform well, the amplitude of the complete gradient was not attenuated as can be seen in Figure 5-11.

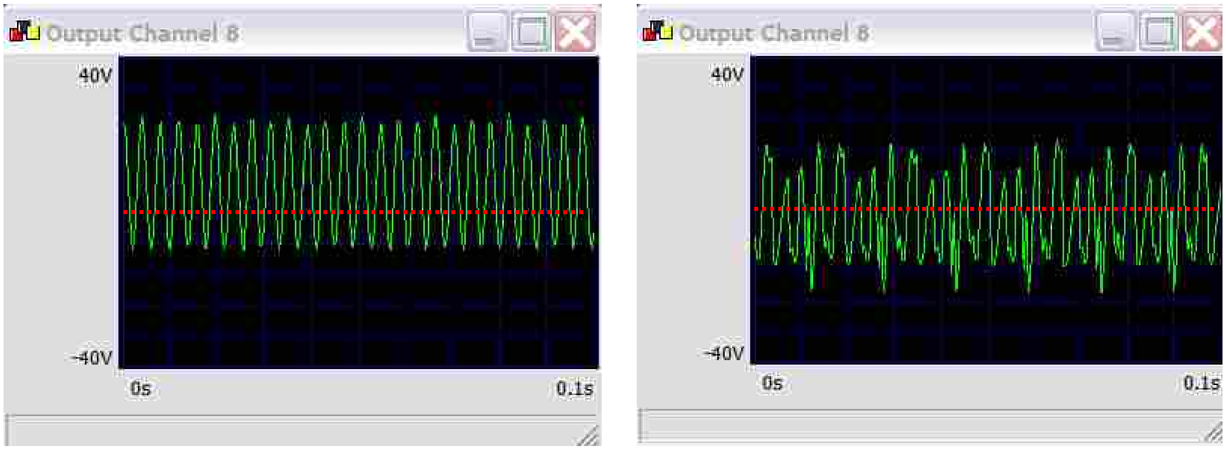

Figure 5-11: Time history of the complete gradient at the (4,2) mode (a) before and (b) after control

The reason that the controller did not converge is because many of the gradient terms were not correlated, which can be explained by the estimate of the transfer function between the controller and the error sensor, $\hat{H}$. A good estimate of $\hat{H}$ needs to be determined otherwise signals will not be correlated, and as a result the objective function will not be attenuated. To explore this phenomenon, two different methods of determining $\hat{H}$ were used and will be explained in the following section.

5.5 Estimate of $\hat{H}$

The initial method used for determining $\hat{H}$ was based on obtaining a broadband response so $\hat{H}$ could be applied to a range of frequencies. In this method, white noise is fed to the control actuator and is sensed by the error sensor configuration. This method uses the cross-correlation between the error and input signals as given in Eq. 5.17 and is based on the block diagram given in Figure 2-1.

$$E\{e(t) * X(t)\} \tag{5.17}$$

In this development, a capital letter symbolizes an array of values with the first value in the array being the current value, followed by past values of the data. An average of the cross-correlation over, in this particular case, 12000 measurements was used. After the averages have been completed, $\hat{\mathrm{H}}$ is updated according to Eq. 5.18.

$$\hat{\mathrm{H}} = \frac{E\{e(t) * X(t)\}}{E\{X(t) * X^T(t)\}} \tag{5.18}$$

While this approach gives a broadband estimate, the accuracy of $\hat{\mathrm{H}}$ at any specific frequency is dependent on the number of taps used, or the length of the filter. If a single frequency is present the filter only needs two taps, theoretically, to determine both the magnitude and phase at the frequency of interest. If, however, multiple frequencies were present more taps would be needed to obtain a more accurate secondary path transfer function model. In this particular case, 120 taps were used to span a frequency range from 0 to 250 Hz. To control squared $\mathrm{V}_{\mathrm{comp}}$, four different $\hat{\mathrm{H}}$ arrays were computed and are given below.

$$\hat{\mathrm{H}}_{\dot{\mathrm{w}}}, \hat{\mathrm{H}}_{\dot{\mathrm{w}}_x}, \hat{\mathrm{H}}_{\dot{\mathrm{w}}_y}, \hat{\mathrm{H}}_{\dot{\mathrm{w}}_{xy}} \tag{5.19}$$

Using only 120 taps for each array and covering a somewhat large frequency range introduced some error and was thought to possibly be the reason for poor control at some frequencies. In order to check this, $\hat{\mathrm{H}}$ for each of the four cases was updated in a separate manner using a simple LMS update. Instead of attempting a broadband approach, a single frequency approach was used in order to more accurately model $\hat{\mathrm{H}}$ at the frequency of interest. It should be noted that while this approach should model the transfer functions better than the broadband approach because all the taps are concentrated on a single frequency, it is only valid for the original driving frequency input and should not be applied to other frequencies, as the control may suffer.

For this method, $\hat{H}$ was updated after every measurement instead of taking the final value after all averages were complete as was done in the previous approach. $\hat{H}$ was updated using the following Eqs. 5.20-5.22.

$$y_j(t) = \hat{H}_j^T X(t) \tag{5.20}$$

$$e_j(t) = d_j(t) - y_j(t) \tag{5.21}$$

$$\hat{H}_j(t+1) = \hat{H}_j(t) + \mu * e_j(t) * X(t) \tag{5.22}$$

where j represents a specific derivative term such as is given in Eq. 5.18 and *d* is the measured value of each of the four terms in squared V_{comp} as given by Eqs. 5.1-5.4. This approach provided a more precise estimate of $\hat{H}$ at the frequency of interest which was expected because all 120 taps were dedicated to a modeling the transfer function of a single frequency. Although the model was more precise than the previous approach, control at 129.0Hz exhibited the same characteristics using this approach although slight improvement were noticed, at least for squared V_{comp} control. Table 5-4 gives the control values using the two approaches at 129.0 Hz.

Table 5-4: Comparison of two techniques for estimating $\hat{H}$

Broadband approach to obtain $\hat{H}$		**Single frequency approach to obtain $\hat{H}$**	
Squared V_{comp} Attenuation	PE Attenuation	Squared V_{comp} Attenuation	PE Attenuation
-8.7	-5.4	-1.4	-4.8
Squared Velocity Attenuation	PE Attenuation	Squared Velocity Attenuation	PE Attenuation
24.7	-0.3	35.2	-8.7

Although squared V_{comp} was still increased when using the single frequency approach, it saw less of an increase and the potential energy followed suit. With a better estimate of the transfer function, velocity was attenuated more, but resulted in increased potential energy in the room, showing that a decrease in velocity at a point does not necessarily result in a decrease in the overall acoustic radiation. Although a more suitable method for determining $\hat{H}$ in accordance with this control technique could possibly be devised, a recommendation to investigate different sensing techniques is given here.

Returning to the comparison between the (2,1) mode and the (4,2) mode, the actual scaled terms of squared V_{comp} will be presented. Realizing that the plate was driven at a single frequency and looking at the terms in real time, each of them should be a sine wave oscillating at the driving frequency. This was the case for the transverse velocity term but not for the other three terms. Although both the x and y rocking terms did exhibit a sine wave with the expected frequency, other frequencies were also present suggesting that errors were introduced. These terms were not able to converge completely. This same effect was more pronounced in the twisting term than the other three. This introduces the fact that the sensing technique employed here introduced errors when dealing with the spatial derivative terms. Finite differencing calculations are sensitive to amplitude errors in the individual signals to be differenced. These errors can be introduced in multiple ways including calibration errors which are direct amplitude errors, positioning errors which would measure the response at a different position and phase differences which would measure the signal at a different instant in time. In the 43.4Hz case, (2,1) mode, because of the placement of the measurement array, the y derivative term dominates the others with the transverse velocity being the next dominant term as can be seen in Figure 5-12.

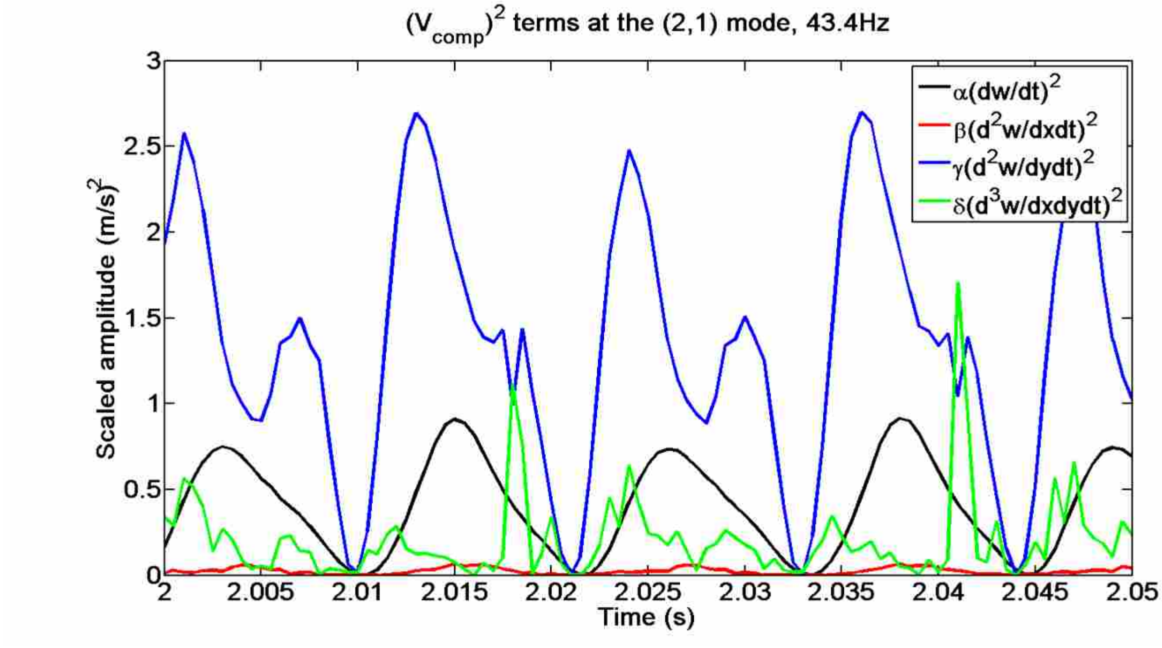

Figure 5-12: $(V_{comp})^2$ terms before control at the (2,1) mode

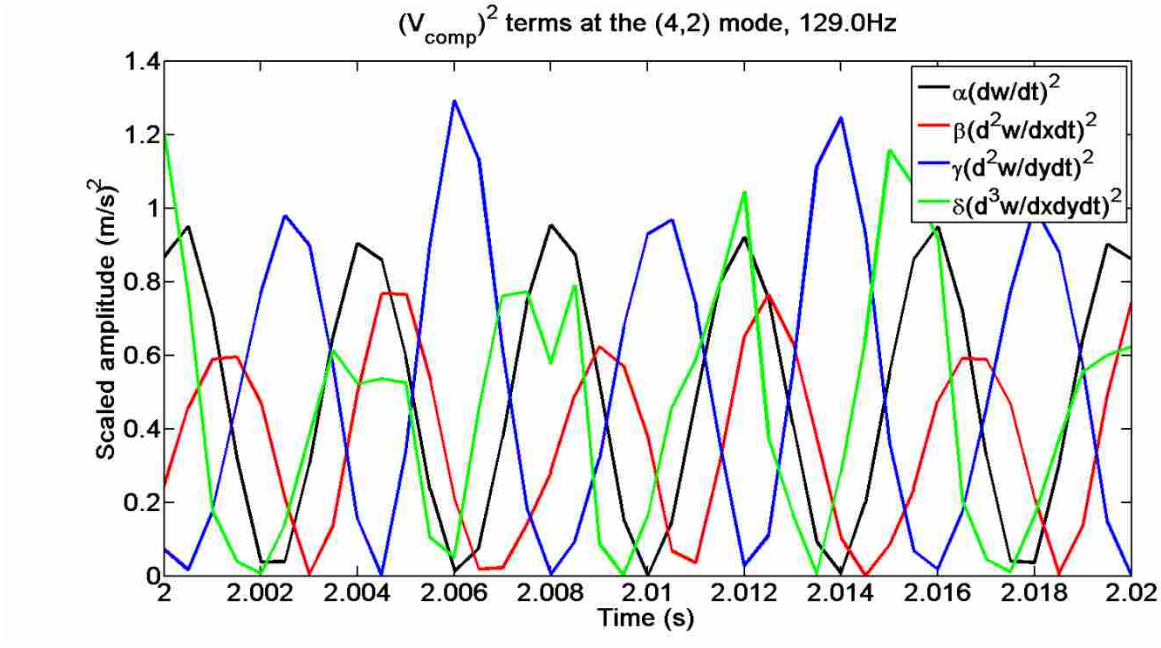

Figure 5-13:$(V_{comp})^2$ terms before control at the (4,2) mode

Although the twisting term at one point does have a large amplitude, it would not be considered significant because the average value is much less than both the transverse velocity and the y-derivative scaled values. Because the twisting terms is not dominant, less error is introduced to the controller via finite differencing. This is not the case with the (4,2) mode at 129.0Hz as can be seen in Figure 5-13. At 129.0Hz, all of the terms are significant which allows the finite differencing errors prevalent in the derivative terms to propagate through to the controller. This is a likely reason that control at 43.4Hz was obtainable and why the 129.Hz case was not able to attenuate squared V_{comp}.

Although the controller was not able to control all frequencies or minimize squared V_{comp} completely, a comparison or ratio of squared V_{comp} attenuation to radiated power or potential energy attenuation should provide a good estimate of whether or not squared V_{comp} control will work experimentally. All the resonance frequencies will be given with a respective velocity control attenuation ratio but only those frequencies for which the controller attenuated squared V_{comp} will an attenuation ratio be given.

In comparing the experimental and analytical values dealing with velocity control, the experimental values were an average of five times lower than analytical cases with a standard deviation of three. This suggests that the attenuation ratios predicted analytical will consistently be lower which is expected as no errors was introduced to the analytical model. The ratios shown in Table 5-5 are given by Eq. 5.23.

$$Attenuation\ ratio = \frac{Structural\ metric\ attenuation}{Acoustic\ attenuation} \tag{5.23}$$

In comparing the experimental and analytical values dealing with velocity control, the experimental values were an average of four times lower than analytical cases with a standard deviation of two when the last mode is eliminated. This suggests that the attenuation ratios predicted analytical will consistently be lower which is expected as no errors was introduced to the analytical model.

Table 5-5: Ratio of squared V_{comp} attenuation to the potential energy radiation comparing experimental and analytical cases

Mode	**Analytical attenuation ratio Velocity Control**	**Experimental attenuation ratio Velocity Control**	**Analytical attenuation ratio $(V_{comp})^2$ Control**	**Experimental attenuation ratio $(V_{comp})^2$ Control**
(1,1)	0.35	0.11	1.49	2.01
(2,1)	0.14	0.03	0.42	0.24
(3,1)	0.35	0.21	1.25	1.79
(1,2)	0.31	0.074	1.05	0.26
(2,2)	-0.09	-0.02	N/A	N/A
(4,1)	0.12	0.01	N/A	N/A
(3,2)	0.10	0.02	N/A	N/A
(4,2)	-0.03	-0.01	N/A	N/A
(3,3)	0.19	0.03	1.05	0.72
(5,2)	0.18	0.07	0.77	0.14
(4,3)/(6,1)	0.11	0.01	N/A	N/A

An important note is that the general trend in the experimental case mimics that of the analytical case. Both the (2,2) and (4,2) modes predicted that with an attenuation in velocity, the acoustic field would see an increase in energy. When looking at squared V_{comp} control, some experimental cases actually performed better than the analytical predictions while others did not perform as well. It was noted, however, that when squared V_{comp} was attenuated at least 1dB, the energy in the acoustic field was also attenuated, suggesting that squared V_{comp} is a beneficial structural control metric.

One explanation as to why the ratios in both the Velocity and squared V_{comp} control cases preformed worse than expected is due to the structural modes present in the experimental plate. Not all the modes which were predicted to show up did, and those that did were not spatially equal to their analytical counterparts. The experimental plate, as previously mentioned, was scanned using an SLDV to determine the resonance frequencies. Two of the resonant modes, as scanned by the SLDV, are shown in Figure 5-14. The analytical predictions were based on clean modes which, as can be seen, do not appear in the experimental test cases which could explain some of the differences between the analytical and experimental results. The skewed modes do not suggest any problem with the plate itself or the experimental setup, it simply suggests that when comparing the ratios, the analytical ratios should not be calculated at the resonance frequencies in Figure 4-2 but shifted a hertz or two.

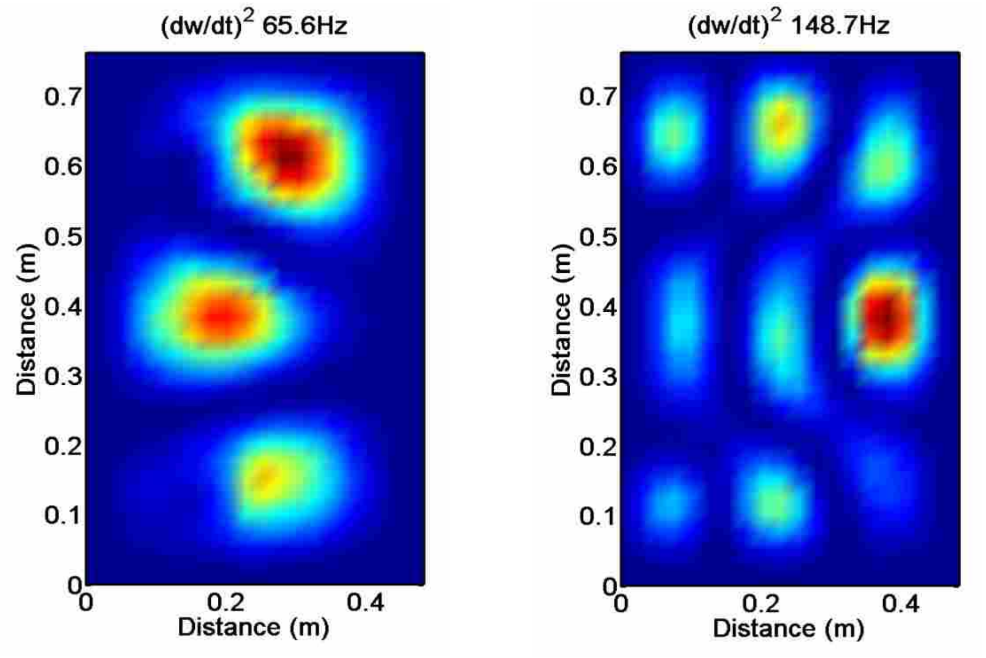

Figure 5-14: SLDV scans of the (1,3) and (3,3) modes

6 RECOMMENDATIONS AND CONCLUSIONS

6.1 Sensor Rotation

The error introduced by the sensor rotation needs to be looked at further. As the acoustic radiation modes have a preferred direction, the sensor should be lined up with this direction as to mimic the radiation modes as close as possible. Also, the optimal α, β, γ, and δ have been solved for taking into account this preferred direction and any deviation from the correct sensor orientation is bound to introduce error. The sensor configuration used is shown in Figure 6-1 and incorporates finite differencing in estimating three of the four values used in squared V_{comp}. The sensor was rotated zero degrees up to fifty degrees from the x-axis as shown in Figure 6-1.

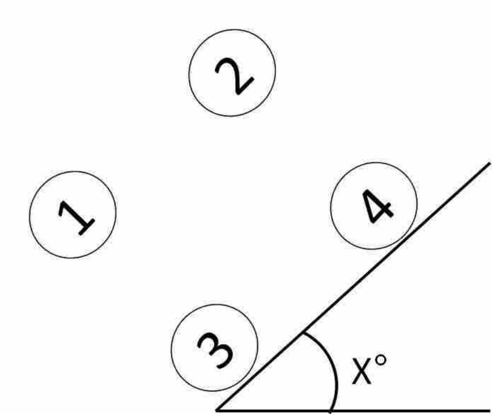

Figure 6-1: Sensor rotation configuration

The same α, β, γ, and δ as are given in Table 3-5 were used in this simulation and the sensor location is the same as given in Table 4-2. Table 6-1 gives the average attenuation over the frequency range of interest for each rotated sensor configuration. The radiated power before and after control with a rotated sensor configuration is presented in Figure 6-2. When the sensor is rotated, it will effectively see different scaling values even though the same numbers will be used because the axes are no longer aligned with the proper x and y axes. As shown in the results, the forty degree sensor configuration actually produced an overall better result than the correctly oriented case.

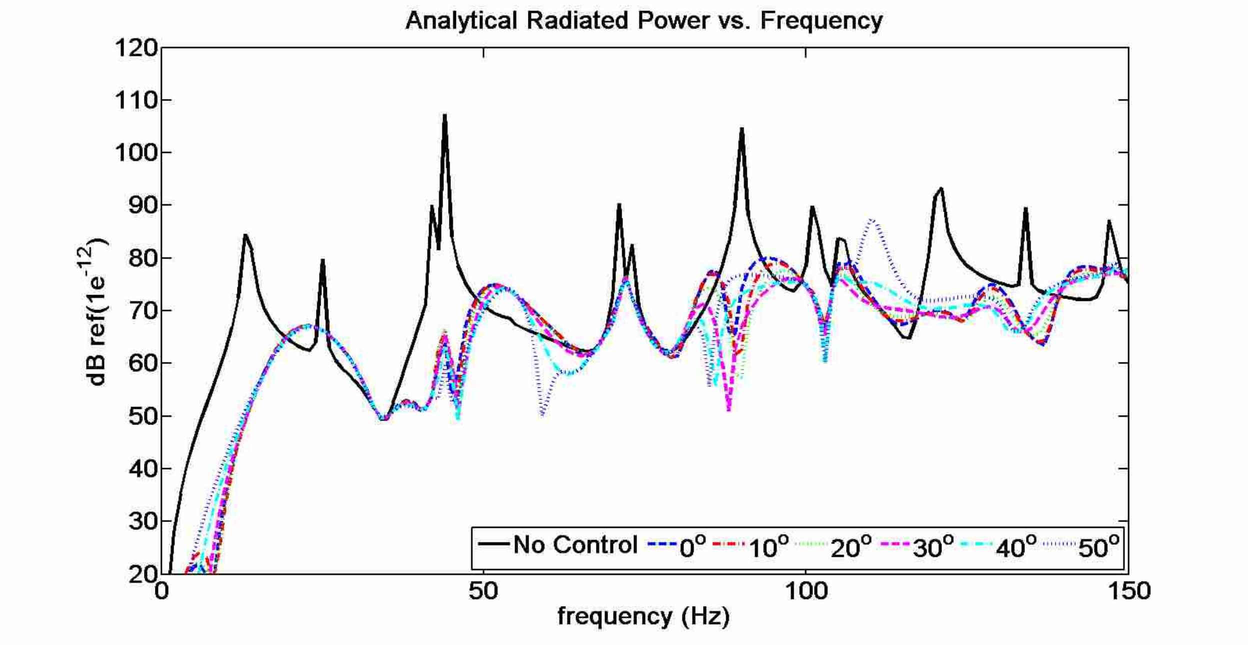

Figure 6-2: Radiated power comparison with a rotated sensor

This suggests that the performance of the objective function is not highly dependent on the scaling values. Not only does this adds to the robustness of the technique, it adds to the practicality as well. In order to get good attenuation overall exact scaling factors do not need to be used. However, if a few dB attenuation overall is of importance, this suggests that there could be a better technique for selecting the best α, β, γ, and δ values than simply averaging the scaling values of the first fifteen structural modes. A better selection could involve a weighted average or possibly an average over all frequencies. As these test cases were run analytically with no noise present, there should not be finite differencing errors introduced as was seen in the experimental measurement array, so these results could be applied to any arbitrary measurement sensing technique.

Table 6-1: Average attenuation with a rotated sensor configuration

Sensor Rotation (degrees)	*Average Attenuation (dB)*
0°	5.8
10°	6.0
20°	6.6
30°	7.2
40°	7.2
50°	5.8

6.2 Measurement Sensing Technique

Another point of investigation would be the measurement array or sensing technique. Because the sensing array given in Figure 5-1, employs finite differencing inherent errors are introduced. More research into the types of sensors which could provide a more accurate determination of the terms in squared V_{comp} which should allow for a better estimate of $\hat{H}$ as was explained previously.

One of the issues which presented itself in the experimental verification was a signal to noise issue. In order to fully understand the benefits of squared V_{comp}, the sensor was placed at locations and frequencies which would provide little to no transverse velocity but a large rocking or twisting term so as to show the success of squared V_{comp} in locations where a point velocity objective function would do poorly. Due to finite differencing and errors introduced by placing the accelerometers on the vibrating plate individually, the separation in x and y varying slightly, squared V_{comp} could not be precisely measured so the control was hindered. For this purpose, an extensive investigation of array types and measurement devices should be completed in order to more fully harness the benefits of squared V_{comp}.

The second reason for creating a better sensing technique is to obtain a better estimate of H for each of the four terms in squared V_{comp} as shown in Figure 5-2. If a more accurate estimate can be acquired, the convergence of the FXLMS algorithm should become better, which in turn would attenuate the objective function, squared V_{comp}, at all frequencies instead of a select few as shown in Figure 5-6.

6.3 Arbitrary Structures

In order for this technique to be applied practically, this method must be able to be applied to most if not all structures. The only change which needs to take place in order to apply this method to all structures requires a simple change in the scaling values. As most structures are not rectangular plates, a simple way to acquire the scaling values, α, β, γ, and δ , must be implemented. In order to examine the plausibility of extending this method to general structures, an analytical model of a circular plate was used in order to verify if a complete and uniform velocity field, or in other words if a uniform squared V_{comp} could be established. Using a model of a clamped circular plate as explained by Fuller[8], the same terms as given in Eq. 3.13 are computed at the (1,1) mode and are shown in Figure 6-3.

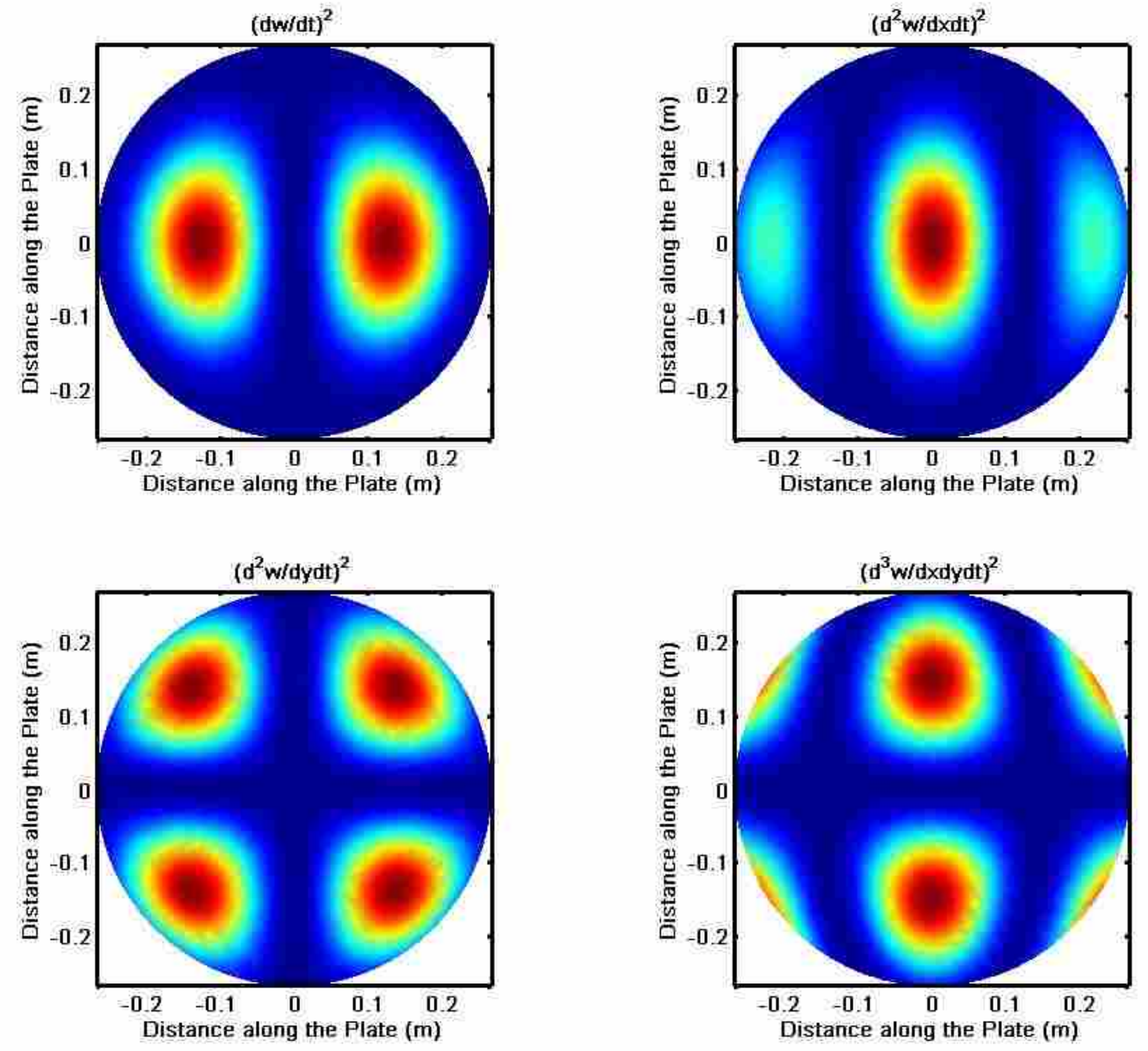

Figure 6-3: Structural components of squared V_{comp} for a circular plate vibrating at the (1,1) mode

The scaling values as computed by normalizing each term in squared V_{comp} are given in Table 6-2 with a visualization of squared V_{comp} given in Figure 6-4.

Table 6-2: Scaling factors for a clamped circular plate at the (1,1) mode

α	β	γ	δ
1	0.006226	0.03128	2.3456e-04

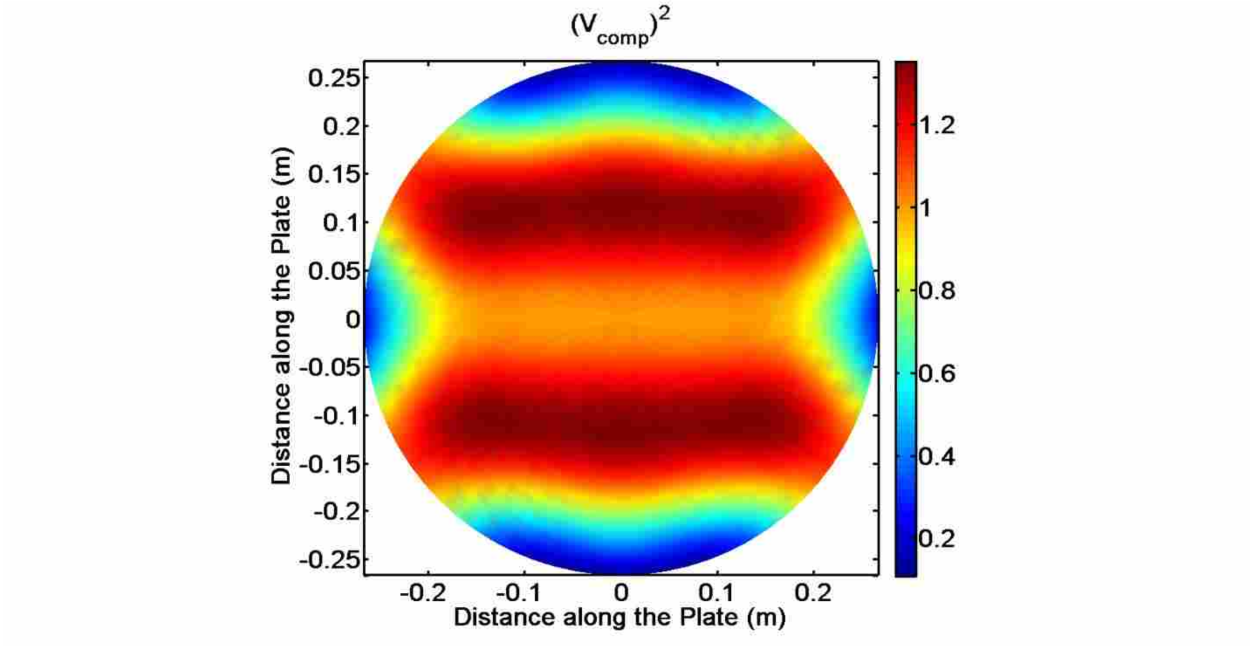

Figure 6-4: Squared V_{comp} for a circular plate

As can be seen by Figure 6-4, squared V_{comp} is not as uniform as the simply supported plate. However, some of this is due to the boundary conditions because for a clamped condition, there will be no bending or twisting at the edges of the plate. Even though squared V_{comp} is not completely uniform, the middle of the plate does become more uniform which again suggests that the sensor not be placed near the edges of the plate. A further investigation into the scaling values is needed in order for this method to be applied to an arbitrary structure. As stated previously, an optimal selection of these values should also be investigated. Although it produced good results when using an average of the first fifteen structural modes in the rectangular panel case, better results would have been obtained had different scaling values been used as was seen in the rotated sensor case.

6.4 Error Possibilities

As this control technique will be investigated further, a list of possible errors which could have affected the performance of the control system are given in Table 6-3. It should be noted that this table does not include all possible sources of error but includes those which could affect the system in the manner noted in section 5.5.

Table 6-3: Possible sources of error

Possible sources of error	Recommendations
Measurement Array	• Create a mechanism which will allow precise positioning of the accelerometers with respect to each other • Investigate alternative methods of measuring the terms in squared V_{comp}
Obtain a better estimate of $\hat{H}$	• Vary the number of SysID taps • Attach he force actuator so no moment will be transmitted to the structure • Determine if the phase on the control actuators creep over time
Hardware and issues	• Understand the hardware used in processing the data, especially the components which acquire the accelerometer signals and output values to the DSP

6.5 Conclusions

Investigating the effects of this new structural velocity quantity, squared V_{comp}, leads to desirable results for the active control of structures. In the analytical cases, the benefits include: control at higher structural modes, control largely independent of sensor location, and need for only a single point measurement of squared V_{comp} with a compact sensor. The control at higher frequencies can be explained by the control of multiple acoustic radiation modes, not just a single one. While all of the desirable characteristics are benefits, the most highly sought after is that of the control being largely independent of sensor location. Strictly speaking, this results in a lack of need for detailed knowledge of structural vibrations before placing the sensor. The overall broadband result of squared V_{comp} control is promising in the area of active structural acoustic control because of the attenuation achieved, lack of dependency on sensor location, and the number of required measurement transducers.

Although these results were not completely verified experimentally, the test cases which were performed offer valuable insights. The experimental cases which produced the desired effect were those cases where the controller converged to a solution and was able to attenuate the objective function at least five decibels. These cases offer validity to the analytical study. At some frequencies the acoustic field saw an increase, but this was due to a poor estimate of the transfer function between the control output and the objective function and did not provide any useful information in regards to squared V_{comp} control. Overall the control of squared V_{comp} produced desirable results, but new sensing techniques need to be explored to more fully validate the benefits of this new structural quantity.

REFERENCES

1. Curtis, A. R. D., Nelson, P. A., and Elliot, S. J. (1988). "Active Reduction of a one-dimensional enclosed sound field: An experimental investigation of three control strategies". *J. Acoust. Soc. Am.,* 2265-2268.

2. Sors, T. C., & Elliott, S. J. (2002). "Volume velocity estimation with accelerometer arrays for active structural acoustic control". *J. Sound Vib.* , 867-883.

3. Johnson, M. E., & Elliott, S. J. (1995). "Active control of sound radiation using volume velocity cancellation". *J. Acoust. Soc. Am.*, 2174-2186.

4. Elliot, S. J., Stothers, I. M., and Nelson, P. A. (1987). "A multiple error LMS algorithm and its application to the active control of sound and vibration". *IEEE Trans. Acoust. Speech Sig.* Process. 1432-1434.

5. Thomas, J. K. (2007). *Secondary path transfer function improvements for enhanced tracking capabilities and convergence of filtered-x LMS based active control algorithms*. Thesis. Brigham Young University.

6. Sommerfeldt, S. D., Nashif, P. J. (1994) "An adaptive filtered-x algorithm for energy-based active control". *J. Acoust. Soc. Am.,* 300-306.

7. Snyder, S. D., Hansen, C. H. (1991). "Mechanisms of Active Control by Vibration Sources". *J. Sound Vib.*, 519-525.

8. Fuller, C.R. (1990) "Active control of sound transmission/radiation from elastic plates by vibration inputs: I. Analysis". *J. Sound Vib.,* 1-15.

9. Fuller, C.R., Hansen, C. H., and Snyder, S. D. (1991) "Active control of sound radiation from a vibrating rectangular panel by sound sources and vibration inputs: An experimental comparison". J. *Sound Vib.*, 195-215.

10. Pan, J., Snyder, S. D., and Hansen, C. J. (1991). "Active control of far-field sound radiated by a rectangular panel-A general analysis". *J. Acoust. Soc. Am.,* 2056-2066.

11. Tanaka, N., Snyder, S. D., Kikushima, Y., & Kuroda, M. (1994). "Vortex structural power flow in a thin plate and the influence on the acoustic field". *J. Acoust. Soc. Am*.1563-1574.

12. Snyder, S. D., Brugan, N. C., & Tanaka, N. (2002). "An acoustic based modal filtering approach to sensing system design for active control of structural acoustic radiation: Theoretical development". *Mechanical Systems and Signal Processing*, 123-139.

13. Elliott, S. J., & Johnson, M. E. (1993). "Radiation modes and the active control of sound power". *J. Acoust. Soc. Am.*, 2194-2204.

14. Cunefare, K. A., Currey, M. N. (1996) "On the exterior acoustic radiation modes of structures". *J. Acoust. Soc. Am.* 2320-2312.

15. Guigou, C., Li, Z., and Fuller, C. R. (1996). "The relationship between volume velocity and far-field radiated pressure of a planar structure". *J. Sound Vib.*, 252-254.

16. Fahy, F., & Gardonio, P. (2007). *Sound and Structural Vibration: Radiation, Transmission and Response.* Oxford: Elsevier.

17. Faber, B. M., Sommerfeldt, S. D. (2006). "Global active control of energy density in a mock tractor cabin". *Noise control engineering journal*. 187-193.

18. Nutter, D. B., Leishman, T. W., Sommerfeldt, S. D., Blotter, J. D. (2007). "Measurement of sound power and absorption in reverberation chambers using energy density". *J. Acoust. Soc. Am.* 2700-2710.